Universiteit Antwerpen

This item is the archived peer-reviewed author-version of:

The properties of SIRT, TVM, and DART for 3D imaging of tubular domains in nanocomposite thin-films and sections

0FThe properties of SIRT, TVM, and DART for 3D imaging of tubular domains in nanocomposite thin–films and sections

Delei Chen[a,b], Bart Goris[c], Folkert Bleichrodt[d], Hamed Heidari Mezerji[c], Sara Bals[c], Kees Joost Batenburg[d], Gijsbertus de With[a], Heiner Friedrich[a,*]

[a] Laboratory of Materials and Interface Chemistry,

Department of Chemical Engineering and Chemistry,

Eindhoven University of Technology, Den Dolech 2,

5612 AZ, Eindhoven, The Netherlands

[b] Dutch Polymer Institute (DPI), P.O. Box 902, 5600 AX, Eindhoven, The Netherlands

[c] EMAT, University of Antwerp, Groenenborgerlaan 171, B-2020, Antwerp, Belgium

[d] Centrum Wiskunde & Informatica, Science Park 123, NL-1098XG, Amsterdam, The Netherlands

* Corresponding author:

  Dr. Heiner Friedrich, Phone: +31-40-247-3041, Email: h.friedrich@tue.nl

Highlights

- Dose and tilt–scheme dependence of SIRT, TVM and DART tomograms are quantified

- SIRT is the most stable method and insensitive to changes in angular sampling.

- TVM significantly reduces noise but objects become thinned

- DART markedly suppresses the elongation artifacts

- No advantage of TVM and DART for fewer projections is observed

Abstract

In electron tomography, the fidelity of the 3D reconstruction strongly depends on the employed reconstruction algorithm. In this paper, the properties of SIRT, TVM and DART reconstructions are studied with respect to having only a limited number of electrons available for imaging and applying different angular sampling schemes. A well–defined realistic model is generated, which consists of tubular domains within a matrix having slab–geometry. Subsequently, the electron tomography workflow is simulated from calculated tilt–series over experimental effects to reconstruction. In comparison with the model, the fidelity of each reconstruction method is evaluated qualitatively and quantitatively based on global and local edge profiles and resolvable distance between particles. Results show that the performance of all reconstruction methods declines with the total electron dose. Overall, SIRT algorithm is the most stable method and insensitive to changes in angular sampling. TVM algorithm yields significantly sharper edges in the reconstruction, but the edge positions are strongly influenced by the tilt scheme and the tubular objects become thinned. The DART algorithm markedly suppresses the elongation artifacts along the beam direction and moreover segments the reconstruction which can be considered a significant advantage for quantification. Finally, no advantage of TVM and DART to deal better with fewer projections was observed.

1 Introduction

Electron tomography (ET) has nowadays become a standard tool for materials research to reveal the three dimensional (3D) morphology of specimens with nanometer resolution [1-4]. Knowledge of a materials 3D morphology is critical to understanding the material properties, such as, e.g., the efficiency of polymer photovoltaic cells [5, 6]. ET consists of three basic steps [2]. First, a series of 2D projections from multiple directions of the object of interest is acquired in a transmission electron microscope (TEM). This is conventionally done by tilting the object over a large angular range at small tilt increments. Second, the series of projections are aligned with respect to a common origin and tilt axis, correcting for unavoidable displacements during data acquisition. Third, the electron tomogram (3D intensity map) of the object is reconstructed from the tilt series by numerical algorithms.

ET is mainly used for qualitative studies where a 3D visualization of different nanostructures is required. Nevertheless a strong trend towards obtaining 3D quantitative information from electron tomograms is ongoing that is currently often hampered by the low reconstruction quality [7]. Several challenges impede obtaining high–quality reconstructions [8-10]. The most significant challenge is that the tilt range for ET is limited (often $< \pm 80°$) because of the sample, the sample holder or the microscope stage [11]. As a consequence, the limited tilt range leads to a missing angular range of information referred to as "missing wedge" [2, 12]. The reconstruction quality is significantly affected by the missing wedge, i.e. elongation in the reconstruction along the beam direction [13]. Another key challenge is the low contrast and low signal–to–noise ratio (SNR) that can be obtained in the projection images, especially for beam sensitive materials [2, 8, 14]. The reason of low contrast is that, e.g., polymers and composites thereof, mainly consist of light elements with small differences in density or composition. In addition, polymers are often very sensitive to electron irradiation and will be shrunk or even bubble during data acquisition if one goes beyond a tolerable cumulative electron dose [15-17]. Therefore, in order to avoid radiation damage and to preserve the structure of the object, only a limited number of electrons can be used throughout data acquisition, thus, leading to low SNR in the projections of the tilt–series.

To overcome the aforementioned challenges, various methods have been proposed in the literature [1, 3, 8]. Instead of a single tilt axis, dual tilt axis has been used during acquisition, thereby reducing the missing wedge to a "missing pyramid" [18, 19]. Nevertheless, the problem of missing information still persists. The ideal tilt range $\pm 90°$ can be reached by fabricating the material of interest into a needle shaped specimen. By mounting the sample in a special specimen holder, an angular tilt range of 360 degrees can be achieved thus completely removing the missing wedge [20, 21]. However, fabrication of a needle–shaped specimen requires materials that are mechanically stable enough which hampers the application to many polymer composites. Finally, to enhance the reconstruction quality, different angular sampling procedures and reconstruction schemes have been suggested and implemented [22-24].

Commonly used reconstruction methods are the weighted backprojection method (WBP) and iterative methods such as simultaneous iterative reconstruction technique (SIRT) [13, 25-27]. The WBP method has been one of the most widely used algorithms [13, 25]. Apart from high computational efficiency, the major advantage of WBP is that the outcome of the reconstruction is thoroughly determined by the experimental data as all steps in the algorithm are linear [13, 28]. However, the main disadvantage of WBP is that the reconstruction quality is sensitive to the limited tilt range [28]. In contrast, the SIRT method generates reconstructions yielding good visual quality from fewer projections and even from noisy data [26, 29]. Therefore, SIRT gradually becomes an increasingly popular reconstruction method used in electron tomography, although it is computationally more expensive. Recently, more advanced reconstruction algorithms have been proposed, such as the discrete algebraic reconstruction technique (DART) [22] and the total variation minimization based reconstruction technique (TVM) [23]. Using prior knowledge of the specimen such as that the specimen contains only a limited number of phases, i.e., a discrete number of gray levels, aids in solving the ill–posed inversion (reconstruction) problem. For example, the DART algorithm actually segments (binarizes) the reconstruction during the iterative process. DART reconstructions are directly quantifiable and have been successfully applied for the 3D characterization of catalytic CuO nanoparticles and zeolite materials [30, 31]. The TVM method is developed based on compressed sensing. It incorporates the prior knowledge that the boundary of the specimen is sparse in the reconstruction [23]. Using this algorithm, the elongation artifacts and

noise in the reconstruction are reduced and the sharpness of the edges is significantly improved. The advantages of the TVM method have demonstrated by the 3D reconstruction of FeO nanoparticles [32] and PbSe/CdSe core–shell nanoparticles [23].

The performance of above advanced reconstruction algorithms have been mainly studied based on experimental data [22, 33] which generally lack the ground truth of the specimens. Nevertheless, some studies have incorporated known phantoms or models into the performance comparison, but these models were based on data that are obtained with a very high SNR in the projections [32, 34, 35]. Hence, no study has included effects of limited electron dose, which we consider the most crucial physical limit to 3D imaging of beam sensitive materials. Thus for beam sensitive materials, detailed studies on the performance of reconstruction algorithms in combination with limited electron dose and varying tilt schemes are lacking.

The aim of this work is therefore to fill this gap by evaluating the fidelity of SIRT, TVM, and DART reconstructions in dependence of a limited total electron dose and a variety of possible acquisition schemes. A comparison to WBP will be presented as a reference. As model structure we focus on the large range of functional nanocomposites composed of tubular domains in a matrix with slab-geometry, i.e. thin-films or thin–sections. Our approach is built on simulating the entire workflow of the bright–field ET from projections, over experimental imaging and recording effects to 3D reconstructions, finalized by a qualitative and quantitative comparison of the initial model and the reconstruction. The reconstruction fidelity is first assessed by image quality. Subsequently, local and global edge profiles and edge spread functions are employed to quantify the resolution in the reconstructions. Moreover, we evaluate the resolvable separation between particles (connectivity and percolation) which is a key question for many functional composites such as photovoltaic bulk heterojunctions or conductive CNT/polymer nanocomposites.

2 Materials and Methods

In this section, we first briefly introduce SIRT, TVM and DART, and then present the simulation approach and evaluation methods [36].

2.1 Reconstruction methods

5

In iterative methods, the reconstructed object is assumed as an unknown array x. According to the measured projections b, a set of algebraic equations can be formulated $Ax = b$, where A is a weighting matrix [23, 25, 26]. The elements of the weighting matrix A represent the contribution of a specific voxel to each projection ray. They can be obtained using different interpolation schemes and thus may yield slight differences in the final reconstruction [37-39]. In order to obtain a reconstruction of the object, x has to be extracted from the projection equation based on a limited data set.

2.1.1 SIRT

The SIRT algorithm is an iterative method based on the algebraic reconstruction technique [25, 26, 29]. The algorithm starts from an initial reconstruction, which is usually obtained by simply assuming a uniform data array or by a simple back–projection from the tilt series. The reconstruction is re–projected along the same tilt angles as the angles used to acquire projections during the experiment, referred as forward projection. The error between the re–projections and the measured projections are calculated and is referred to as "projection error", and then simultaneously back–projected to refine the reconstruction. This process is iterated until a stop criterion is reached, conventionally the number of iterations. Using this method with few iterations, the noise in the reconstruction can be suppressed, yielding good looking reconstructions.

2.1.2 TVM

As mentioned above, TVM in the used implementation is an iterative method based on compressive sensing [23, 33]. It assumes that the specimen has only a few components and that the gradient of the specimen is sparse. Based on this sparsity assumption, the aim of TVM is to find the reconstructed object which has a minimum norm of the discrete gradient, i.e. the total variation. This method is implemented by simultaneously minimizing the projection error and the total variation of the reconstructed object, and can be represented by:

$$\hat{x} = \arg\min_x \left[TV(x) + \frac{\mu}{2} \|Ax - b\|^2 \right] \tag{1}$$

where the *TV(x)* is the total variation of the reconstructed object *x*, μ is a regularization parameter, and $\|\circ\|^2$ denotes a sum of squared difference. The projection error is represented by $\|Ax\text{-}b\|$. As can be seen from this equation, the regularization parameter μ is very important. A large value of regularization parameter μ will result in a quasi–SIRT reconstruction, in which artifacts from noise and the missing wedge may be preserved. A small value of μ will reduce noise in the reconstruction, but small features in the object will also be removed. Therefore, great care should be taken when choosing the value of the regularization parameter. Although the ground truth is known in the simulation experiments performed in this work, this knowledge is not incorporated when estimating a correct value for the penalty parameter yielding a more realistic workflow.

2.1.3 DART

DART is an iterative algorithm that was developed for objects which consist of only few materials, corresponding to a few distinct grey levels in the reconstruction [22, 40]. This prior knowledge is combined with a continuous iterative reconstruction algorithm (such as SIRT) by introducing a discretization step. The algorithm starts from a SIRT reconstruction to obtain information of grey levels in the reconstructed object. A threshold is then selected and applied to segment the reconstruction. Boundary pixels are detected from the segmented reconstruction, which are all pixels that have at least one neighboring pixel in a different segmentation class. The remaining pixels are referred as non–boundary pixels, and they are assigned to the grey levels that correspond to either background or objects. Afterwards, the SIRT method is employed again, but only boundary pixels are updated in each iteration step. The non–boundary pixels remain fixed throughout this process. In this way, the number of unknown pixels is extremely reduced. The update of the boundary is repeated until the method converges. In the end, a reconstruction is obtained, which is segmented and can be used for further quantification of structural properties.

2.2 Simulation approach and Evaluation methods

In this section, we will introduce our simulation approach and the evaluation methods [36]. As shown in Figure 1, the entire simulation contains of four steps: model

7

definition, image formation and recording, reconstruction, and quantitative comparison.
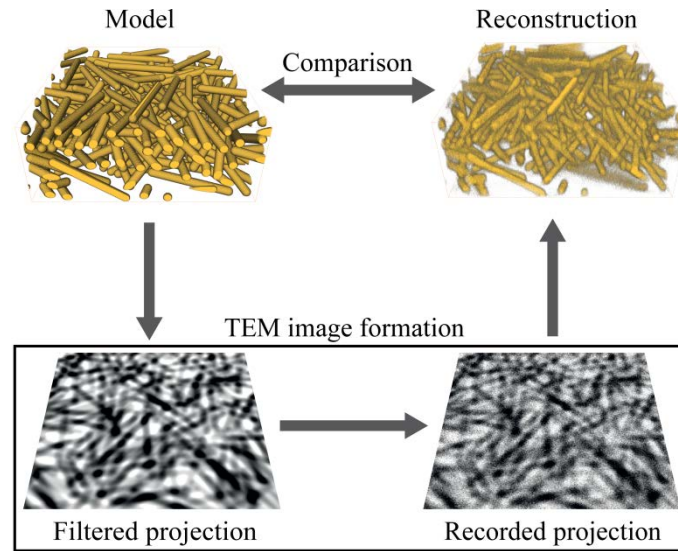

Figure 1. Flowchart of the simulation approach. First, a well–defined model system is generated, which consists of a polymer matrix and rod–like nanofillers. Second, TEM images of the model are calculated based on mass-thickness contrast with a low–pass filter and noise. After calculating the tilt series, reconstruction is carried out. In the end, qualitative and quantitative comparisons of the reconstruction to the model are implemented to investigate the performance of reconstruction algorithms.

2.2.1 Model definition

Our model approximates the structures of a large range of functional nanocomposites, such as a bulk heterojunction composed of P3HT nanowires in a PCBM matrix[6, 41] or carbon nanotubes in a polymer matrix [42].The ingredients of the model system therefore consist of a polymer matrix (background) having a slab–geometry and rod–like nanofillers (object), as can be seen in Figure 1 and Figure S1. The rod–like filler, such as P3HT nanowires and carbon nanotubes, is simplified to a cylinder with spherical end caps which has a 200 nm length and 20 nm diameter. The thickness of the matrix is 200 nm as conventionally prepared by spin coating (bulk heterojunction) [6] or by (Cryo–)ultramicrotomy (CNT composite) [43]. In order to bridge the realms of medium resolution cryo–electron tomography to high resolution 3D imaging, the sampling in the model is set to 1 nm/pixel, which we used often in our experimental work.

2.2.2 Image formation

Our image formation model includes three main steps in electron microscopy: electron–specimen interaction, the optical system, and the recording process [44-46].

As an incident beam I_0 passes through a specimen with thickness t, the number of transmitted electrons owing to electron–specimen interaction decreases exponentially as a function of object thickness: $I_t = I_0 \exp(-t/\Lambda_t)$, where Λ_t is the mean–free–path (MFP) length of the specimen [46, 47]. The ideal projection formed by the transmitted electrons is transferred by the electron optical system of the TEM into the detector plane. In cooperation with aberration of the objective and defocus used for imaging, the optical system is modeled as a low–pass filter in first approximation. The transferred projection is thus simulated by the ideal projection with this low–pass filter, referred as filtered projection. Finally, the filtered projection is recorded by the TEM electron detector, i.e., a charge–coupled device (CCD) camera. The recording process introduces shot noise and CCD noise [48-50]. The intensity of the final projection is calculated by adding both shot noise and CCD noise to the filtered projection. More details can be found in the Supplementary Information (SI), Section 1.2.

2.2.3 Acquisition parameters and reconstruction

In order to assess the ability of reconstruction methods dealing with noise, especially for beam sensitive polymer composites, we employ three different total electron doses I_{total}, which roughly correspond to electron doses commonly employed for cryo–ET of vitrified specimens in their native liquid condition (highly beam sensitive, 10^2 e/Å^2), for polymers and composites thereof (beam sensitive, 10^4 e/Å^2), and for inorganic materials (least beam sensitive, 10^6 e/Å^2). For each projection in the tilt series, an equal incoming electron I_0 dose is assumed, i.e., $I_0 = I_{total}/N$, where N is the number of projections, thus, not taking a dose distribution factor into account. To investigate the influence of the angular sampling scheme, three different tilt increments $\Delta\theta_0$ are studied, i.e. 1° and 5° constant increments, and Saxton scheme of 3° as starting increments at zero degree tilt angle [51]. The maximum tilt range is ±65°, which is commonly used in ET. The main acquisition parameters are listed in **Table 1**.

Table 1: TEM parameters and acquisition schemes used for calculating projections

Parameter	Value
Acceleration voltage (keV)	300
Underfocus (μm)	−5
Total electron dose (e/Å^2)	10^2, 10^4, 10^6
Tilt range	±65°
Tilt increment	Constant increment: 1°, 5°, Saxton scheme: 3°

The resulting nine tilt–series were reconstructed by SIRT, TVM and DART. In the SIRT reconstructions, the number of iteration was 10, 50, and 100 for accumulated electron dose of 10^2 e/Å^2, 10^4 e/Å^2, and 10^6 e/Å^2, respectively. More details on SIRT reconstructions and how the iteration number was selected can be found in the SI, Section 1.3. In the TVM approach, the regularization parameter μ was optimized for each reconstruction based on visual inspection. This is by no means the best approach but commonly done as better defined criteria are often lacking [52]. The standard DART algorithm is utilized with 100 iterations for all the reconstructions [22, 40], and a global threshold is used for segmentation which is set to the average value (0.5) of the background (0) and the particle intensity (1). The volume size for each reconstruction is 508×508×200 voxels.

2.2.4 Evaluation methods

Several methods have been proposed to estimate the resolution in ET but no straightforward widely accepted approach exists [53-57]. If the reconstruction is from a tilt series with a tilt range of ±90° around a single–tilt axis (Y direction), the attainable resolution has been estimated to $d_X = \pi D/N$ along the X direction [53], where D is the diameter of the object and N is the number of projections. Nevertheless, the limited tilt range in the ET leads to the elongation along the beam direction Z in the reconstruction. Therefore, the resolution in the Z direction d_Z is degraded by an elongation factor e_{xz} which is a function of the maximum tilt range α [58]:

$$d_z = d_x e_{xz} = d_x \sqrt{\frac{\alpha + \sin\alpha\cos\alpha}{\alpha - \sin\alpha\cos\alpha}} \qquad (2).$$

Obviously, above descriptions of the resolution is only based on sampling considerations. Since noise and blurring also influence the achievable resolution in the reconstruction, they need to be considered as well.

In the present work, edge intensity profiles that encode the effects of dose, imaging and processing have been used to determine the resolution and, thus, the quality of the reconstruction [36, 56]. An edge intensity profile is taken across the background–object edge transition with equal numbers of pixels on each side, which is 20 pixel long and 1 pixel wide (Figure 2). The intensities of the ideal edge profile (Figure 2b–Ideal) in the model only contain two grey levels: background (0) and objects (1), and the transition occurs at the 10.5 pixel position, referred to as the edge position. These ideal profiles are broadened and become noisy after reconstruction (Figure 2b–Local). More detailed information about the reconstruction, such as the dynamic range a, the background intensity b, the edge position x_0, and the edge steepness k, can be obtained from characterization of the reconstructed edge by looking at the reconstructed profiles. To quantify the edge profiles, an edge spread function (ESF) is defined including the above mentioned four parameters.[36, 56] Mathematically, it can be represented by a continuous sigmoidal function [59],

$$S(x) = \frac{1}{2}a\left[1 + \left(\tanh\left(k(x - x_0)\right)\right)\right] + b \tag{3}$$

In order to find the four unknown parameters, the ESF is fitted to the edge profiles. The resolution in the reconstruction can be defined by the full–width–at–half–maximum (FWHM) of the first derivative of the edge profiles, which is the inverse of the steepness k: $\Delta r = 1.76/k$. In other words, the steepness k is the resolution in the frequency space. In order to assess the reconstruction quality globally and locally, we define two types of edge profiles: a local edge profile which is an individual edge intensity profile taken directly from a reconstruction with 20 pixel length and 1 pixel width, and a global edge profile which is obtained by averaging all the local edge profiles in the same direction in a reconstruction.
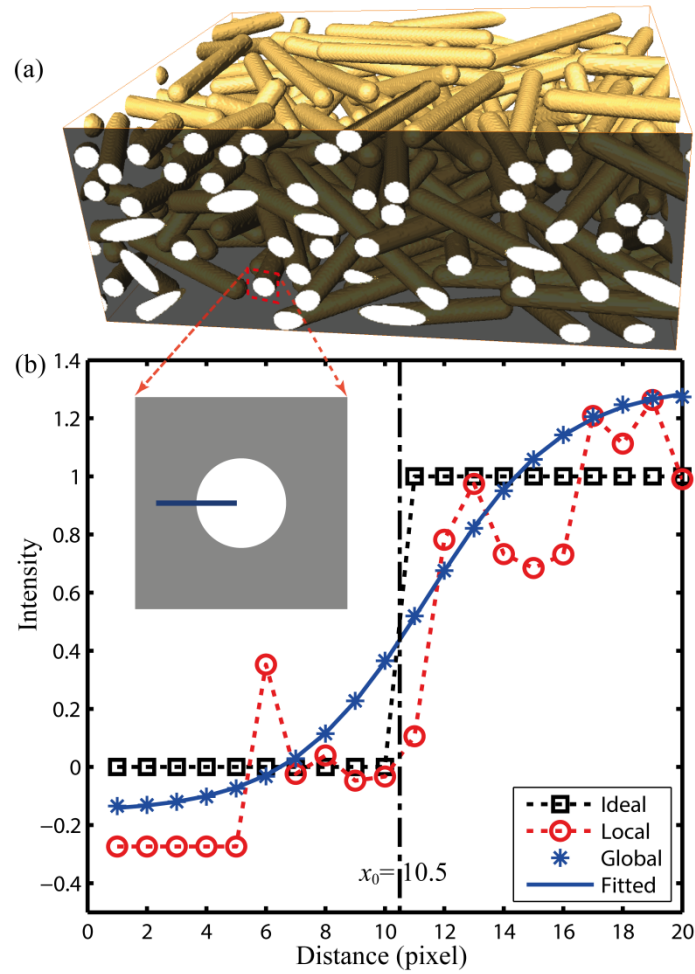
Figure 2. Illustration of the edge intensity profile from the model, which is taken across the background–object interface. An ideal edge intensity profile is a step profile, 20 pixels long and 1 pixel wide, thus the edge position is at 10.5 pixel (indicated by the middle vertical line). A local edge profile is taken from the reconstruction, and a global edge profile is obtained by averaging all the local edge profiles in the same direction. An edge spread function is fitted to the edge profiles to evaluate the quality of the reconstruction.

Apart from particle size, the connectivity of objects throughout a volume is of great interest, as it is often closely related to the functional properties of specimens, e.g., conductive network of CNT's in the polymer nanocomposites. Henceforth, we carry out such an analysis and study the resolvable separation between particles by comparing the intensity profiles across gaps of varying size, referred to as gap intensity profiles.

A gap intensity profile is a line intensity profile which is taken from one particle over the background to another particle, as depicted in Figure 3. Using a similar procedure as for obtaining the global edge profile, a global gap profile is calculated by averaging over all local gap profiles with the same gap width taken from a reconstruction in the same direction. In this manner, each reconstruction yields three global gap profiles,

along the X, Y and Z direction, respectively. In order to find the resolvable separation, an inverted Gaussian function is fitted to the global gap profiles, and the gap width is determined by the full–width–at–half–maximum (FWHM) of the fitted Gaussian. To probe for actually resolvable distances between two particles in a reconstruction, four different gap widths were chosen, i.e. 3 nm, 6 nm, 9 nm, and 12 nm.
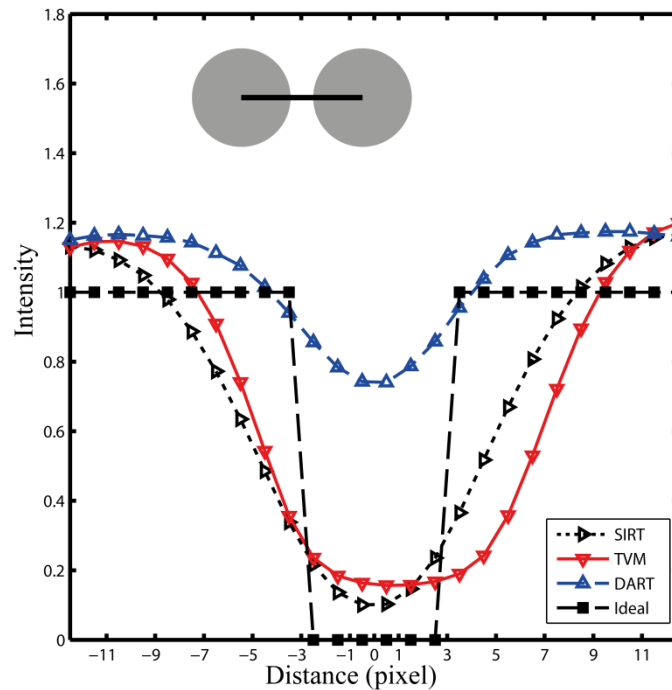

Figure 3. Illustration of the gap intensity profile, which is taken from one particle side over a background to another particle side. Besides the ideal gap profile with a 6 pixel gap from the model (square), an example global gap profile for a SIRT (right triangle), TVM (down triangle), and DART (up triangle) reconstruction along the X direction are shown.

3 Results

In the following, we present visual inspection (3.1), evaluation based on global edge profiles (3.2), local edge profiles (3.3), and gap profiles (3.4). The projections were also reconstructed using WBP as reference for quantitative analysis. Further details on the WBP parameters can be found in the SI, Section 1.3. For the purpose of visualization, all the reconstructions are normalized to the same mean density. The normalization method is presented in the SI, Section 2.1.

3.1 Reconstruction results

The fidelity of the reconstructions is first visually inspected in comparison with the model. As shown in Figure 4, there are no significant differences between SIRT, TVM and DART reconstructions at a cumulative electron dose of 10^2 e/Å^2. All reconstructions (Figure 4 and S3) suffer from high noise contributions, leading to low visibility of the rods. Here SIRT and DART show no directionality of features in the XY plane while TVM shows a characteristic horizontal striping which is a result of breaking up the full 3D dataset into $N\times$2D reconstructions. Although the white bands on the left and right of the numerical TVM cross-sections do change the absolute intensity of the features, they do not affect the quantification. (See SI, Section 2.1 and 2.2 for a discussion of the effects on quantification).
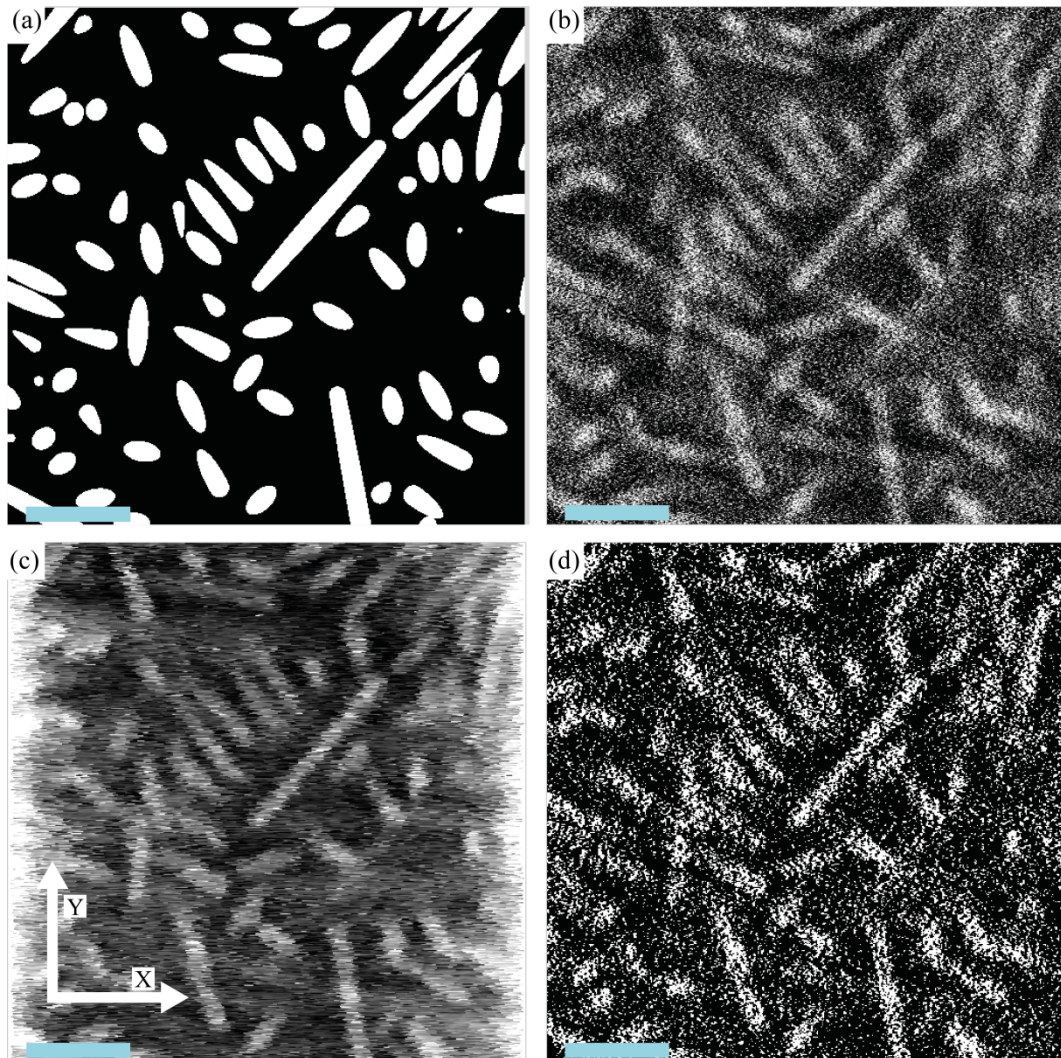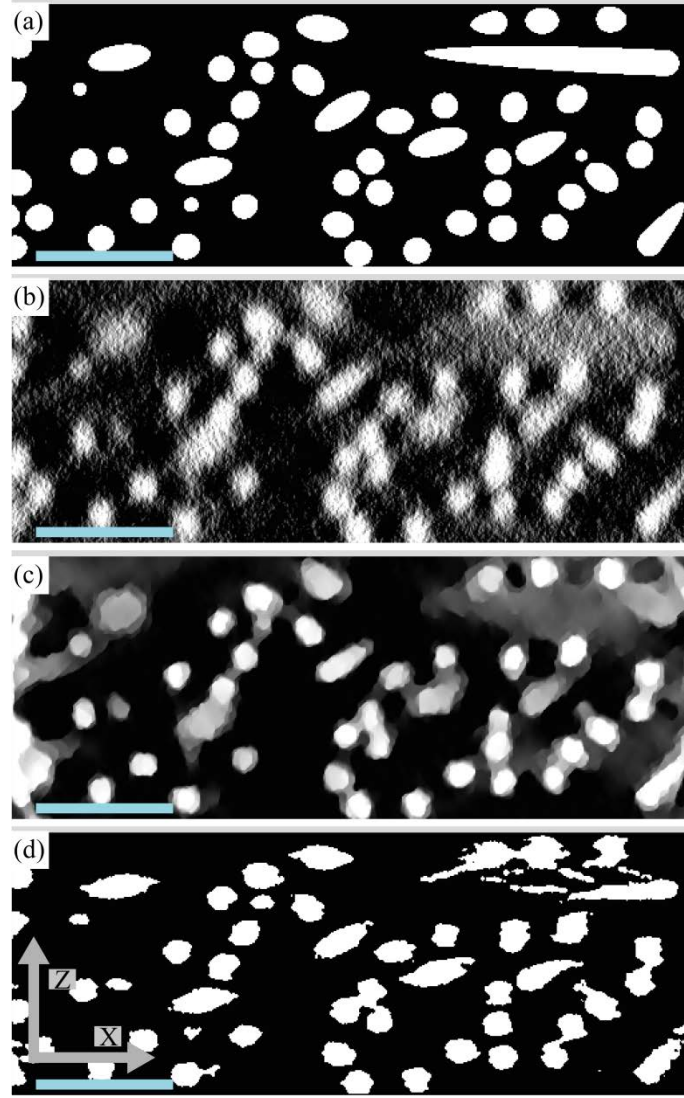

Figure 4. An XY numerical cross section through the model (a), the SIRT (b), the TVM (c), and the DART (d) reconstructions using the total electron dose of 10^2 e/Å^2, and a tilt increment of 1°. Scale bars are 100 nm.

As expected, reconstructions are notably improved by increasing the total electron dose to 10^4 e/Å^2 (Figure 5) and 10^6 e/Å^2 (Figure S4). Compared with the model, it can be seen that particles in the SIRT reconstruction (Figure 5b) are elongated due to the missing wedge, but in the TVM reconstruction (Figure 5c) the tubular domains seem thinned, a point that will be further discussed in paragraph 3.2.2. Moreover, neither SIRT nor TVM algorithms can properly resolve objects whose long axis is perpendicular to the beam direction Z and the tilt–axis Y. The same holds true for the DART algorithm where objects oriented along the X axis are sometimes but not always reconstructed (unstable behavior). Nevertheless the DART algorithm significantly suppresses the elongation artifact along the beam direction (Figure 5d) and separates neighboring objects well. A 3D volume rendering of these results is shown in Figure S5 in the Supplementary Information, illustrating the advantages of TVM and DART on account of the lowered noise in the reconstruction.

Figure 5. An XZ numerical cross section through the model (a), the SIRT (b), the TVM (c), and the DART (d) reconstructions using the total electron dose of 10^4 e/$\mathring{A}^2$ and a tilt increment of 1°. Scale bar is 100 nm.

3.2 Global edge profiles

In the following, the transitions between tubular domains and matrix in SIRT, TVM, and DART reconstructions will be quantitatively evaluated. Utilizing the edge spread function, we first quantify the quality of reconstructions globally. In each reconstruction, three global edge profiles along the X, Y, and Z directions are calculated by averaging all the local edge intensity profiles along the same direction. Subsequently, the edge spread function given by Equation (3) is fitted to all the global edge profiles. The global edge profiles and the corresponding fitted profiles along both the X and Z directions are plotted and presented in Figure S6 and S7. The

16

standard errors of the steepness and the edge position and the goodness–of–fit (R^2) are listed in Table S2.

Figure 6 shows the results of the fitting process focusing on the edge shift ($\Delta x_0 = x_0 - 10.5$) and the steepness (k) as a function of tilt increments and dose. For completeness, the corresponding results using WBP are also presented in Figure 6. For convenience, the edge position x_0 is replaced by the edge shift Δx_0, which is the displacement of the edge position in the reconstruction as compared to the model. A negative edge shift means the edge moves to the background side which leads to an increase in object volume, while a positive edge shift indicates that the edge moves into the object side which results in a decrease of the object volume. In the following, we will discuss the results for each algorithm in terms of dose and the acquisition scheme.

3.2.1 SIRT

As shown in Figure 6a,b, the edge position in the SIRT reconstructions along the X direction are positively shifted (0.5 to 1.0), whereas along the Z direction are negatively shifted (−0.5 to −1.0) for all the acquisition schemes. Despite of the measured edge shifts, effects of the total electron dose and tilt increments are absent, rendering the algorithm insensitive and stable with respect to changing acquisition conditions. The steepness k in SIRT reconstruction generally increases from 0.17 (10^2 e/Å^2) to 0.21 (10^4 e/Å^2) to 0.23 (10^6 e/Å^2) along the X direction, while from 0.13 (10^2 e/Å^2) to 0.16 (10^4 e/Å^2) to 0.17 (10^6 e/Å^2) along the Z direction, as shown in Figure 6c,d. This dose effects become clearer when looking at the spatial resolution Δr which changes, for example, from 13.5 nm (10^2 e/Å^2) to 11.1 nm (10^4 e/Å^2) to 10.4 nm (10^6 e/Å^2) along the Z direction. At equal total electron doses, the steepness k in the X direction is independent of the tilt increments (Figure 6c). Along the Z direction (Figure 6d) slight variations are observed such that the resolution using a Saxton 3° tilt–scheme is approximately 0.5 nm better than using 1° increment, and 1 nm better than using 5° increments. The elongation factor e_{xz} determined from the z vs x size of the rods at the electron dose 10^2 e/Å^2 is about 1.25, and 1.37 at both the electron dose of 10^4 e/Å^2 and 10^6 e/Å^2, less than the value predicted for the elongation of the WBP point–spread function i.e. $e_{xz} = 1.42$ [58].
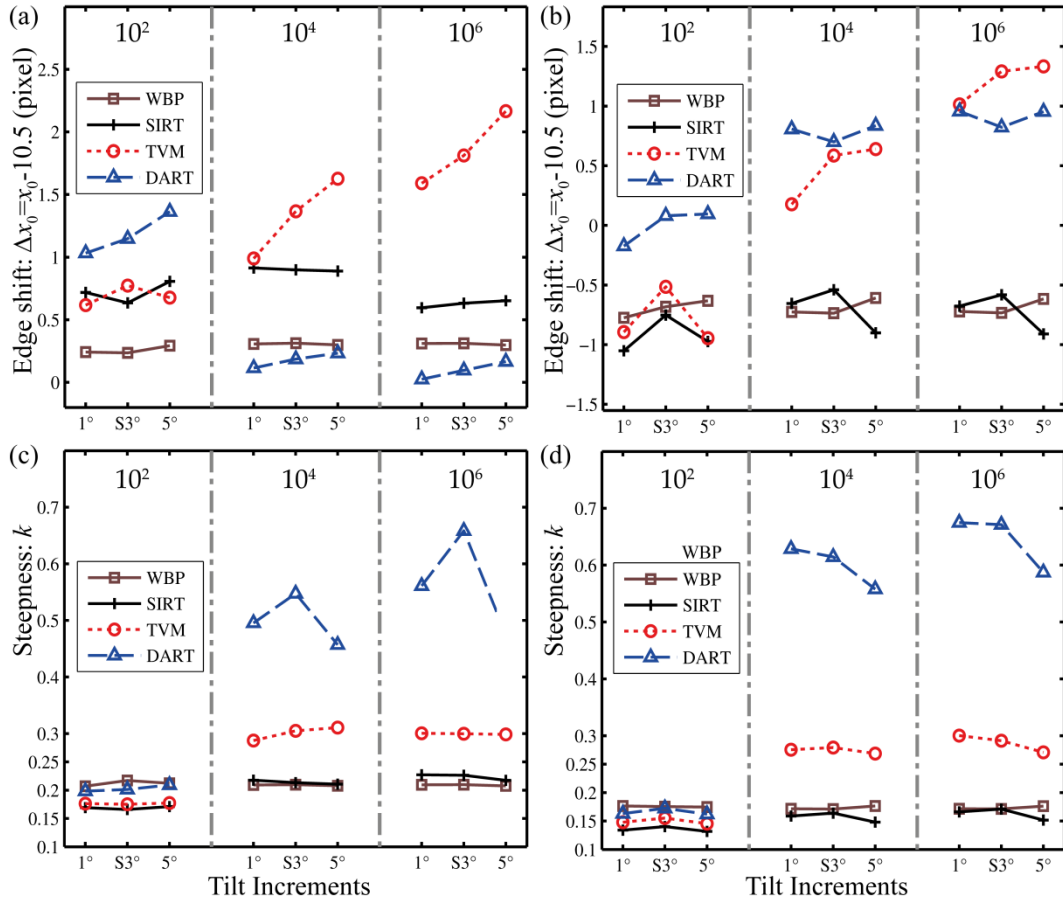
Figure 6. Edge shift and steepness of global edge profiles along the X direction (a, c) and the Z direction (b, d) in the reconstruction at the total electron dose of 10^2 e/Å^2, 10^4 e/Å^2, and 10^6 e/Å^2. Edge shift (a, b) is the difference of the edge position between the model and the reconstruction. A negative edge shift means the edge moves to the background side, while a positive edge shift means the edge moves to the object side. The standard parameter errors can be found at Table S2 in the Supplementary Information. S3° denotes the Saxton scheme with an angular starting interval of 3°.

3.2.2 TVM

In the TVM reconstructions, the measured edge positions are strongly influenced by the tilt increments and the total electron dose (Figure 6a,b). Similar as for SIRT, at a total electron dose of 10^2 e/Å^2, the edge position in the X direction is positively shifted, while in the Z direction it is negatively shifted. In both directions, the edge shifts are less than 1.0 nm, regardless of the tilt increments. For higher electron doses, the edge position is still positively shifted but further away from the original position in the X direction, whereas in the Z direction the edge shift becomes positive. It is interesting that the edge shift is increasing with increasing tilt increments in both X and Z directions, indicating that the compressed sensing approaches is significantly influenced by the tilt increment when a limited electron dose is used. This is contrary

18

to previous results where compressive sensing based approaches are used for the reconstruction of nanostructures based on high–angle annular dark–field STEM tilt series with a higher SNR [23, 35]. As a consequence of the observed edge shifts, the size of objects will be underestimated. For example, the volume of a sphere with a 10 nm radius will be reduced by 20%, taking the edge shift from the reconstruction at the total electron of 10^4 e/Å^2 with the Saxton 3° tilt increments into account. However, it must be noted that this underestimation may be largely influenced by a non–optimal choice of the regularization parameter. Changing this parameter will yield large differences and may even result in an overestimation of the observed edge shift. Therefore, obtaining an objective approach for determining the optimal penalty parameter may be crucial in order to obtain accurate quantitative results.

The steepness, i.e. resolution, in the TVM reconstruction mainly depends on the total electron dose (Figure 6c,d), improved from 0.18 to 0.30 in the X direction and from 0.15 to 0.28 in the Z direction for 10^2 e/Å^2 and 10^4 e/Å^2, respectively. Only minor improvements in steepness are observed from 10^4 e/Å^2 to 10^6 e/Å^2. TVM, as for SIRT and WBP, shows only slight changes with tilt increments, and the values for X and Z only slightly differing resulting in a rather isotropic resolution for this limited ±65° tilt–range.

3.2.3 DART

The observed edge positions in DART reconstructions are mainly related to the total electron dose (Figure 6a,b). At the electron dose of 10^2 e/Å^2, the edge position in the X direction moves to the inside of the object and the shift slightly increases from 1.03 nm to 1.15 nm to 1.36 nm as the tilt increments change from 1°, to Saxton 3°, to 5°. It is interesting that, however, the edge shift in the Z direction is negligible, −0.17 – 0.1, which indicates the elongation effect owing to the missing wedge has been suppressed. At total electron doses of 10^4 e/Å^2 and 10^6 e/Å^2, positive edge shifts in the both X and Z directions are observed. The edge position in the X direction is close to the original position, whereas in the Z direction it moves ~ 0.85 nm to the inside of the object, as shown in Figure 6a,b. Overall, only a minor influence of the tilt increments on the edge positions are found.

While individual edge profiles in the DART reconstruction are step profiles on account of the binarized reconstruction, the global edge profile nevertheless is an

average of overall local edge profiles, and thus the global steepness mainly represents uncertainty in local edge positions. Hence, as displayed in Figure 6c,d, a steepness of the global edge smaller than 0.8 is obtained. This is significantly larger than for all other reconstruction approaches and highlights the uniqueness of the method. We will discuss the distribution of local edge positions in the next section.

3.2.4 WBP

From Figure 6, it can be seen that both the edge position and the steepness of the global edge profiles from the WBP reconstruction are barely influenced by the changes of the total electron dose and the sampling schemes. The reason is that the procedure of gaining the global edge profiles by averaging over approximately a million edge profiles leads to virtually noise–free global edge profiles, though the SNR of the reconstruction strongly varies with changes of the total electron dose. The edge shifts in the X direction are negligible, whereas in the Z direction they are shifted to the background side. As expected, the steepness along the X direction (ca. 0.21) is larger than along the Z direction (ca. 0.17). The resulting elongation factor, i.e. $e_{xz} = 1.21$, is smaller than the theoretical value for the WBP PSF (1.42). Overall, the performance of WBP is in line with more advanced approaches looking at the global edge profile alone. For more details about the performance of the WBP reconstruction in terms of the limited electron dose and the acquisition schemes, we refer to reference [36].

3.3 Local edge profile

Since the global edge profiles are averages of all local edge profiles, characterization of such profiles mainly reveals overall trends in reconstruction quality. Nevertheless, dose related properties are mainly encoded in the local edge profiles. To gain further knowledge about the behavior of the three reconstruction algorithms in terms of the total electron dose, we focus in this section on the statistical characterization of local edge profiles. To this end, first an edge spread function is fitted to the local edge profiles along the X, Y, and Z directions separately. Second, the probability density distributions of the edge shifts from each reconstruction are obtained and analyzed statistically. Note that it is not appropriate to compare the steepness in the DART reconstruction with the steepness in the SIRT and the TVM reconstruction, as the

individual edge profile in the DART reconstruction is a binary profile and therefore the steepness is infinitely large. A detailed description of the fitting procedure can be found in in the SI, Section 2.4 and Figure S8.

Figure 7 shows the probability density distribution of edge shifts along the X direction in the SIRT, TVM, DART, and WBP reconstructions, whereas Figures S9 and S10 present the corresponding distributions along the Z and Y direction, respectively. The corresponding population mean, standard error of population mean and standard deviation are shown in Table S3. Since the standard error of the population mean is significantly smaller than the differences in edge shift between different reconstructions (see table S3), observed differences in edge shift are significant and interpretable. In general, it is observed that the probability distribution of the edge shifts in each reconstruction becomes wider (increasing standard deviation) with a decreasing total electron dose.

In the SIRT reconstruction, at an electron dose of 10^6 e/Å^2 (Figure 7a), the distribution of edge shifts in each direction is a quasi–Gaussian distribution which its mean closes to the corresponding global edge shift. Compared to the distribution of the edge shift in the X direction with the standard deviation $\sigma_x \approx 1.69$ nm, the distribution in the Z direction (Figure S9a) is considerably wider ($\sigma_z \approx 2.30$ nm), reflecting the effect of the missing wedge. As the total electron dose decreases to 10^4 e/Å^2 (Figure 7b), the probability distribution of the edge shifts is still a quasi–Gaussian distribution but broadened further, e.g., with $\sigma_x \approx 2.23$ nm standard deviation for the X direction. At the lowest electron dose of 10^2 e/Å^2 (Figure 7c), however, the probability distribution of the edge shifts becomes a uniform distribution, leading to a large variation in determination of edge positions, e.g. $\sigma_x = 3.50$ nm. Consequently, the reliability of measurements, such as object size, will be very low. For instance, assuming a sphere of 20 nm in diameter reconstructed at a total dose of 10^2 e/Å^2, and considering the uncertainty along both X, Y and Z direction given by the standard deviation of the distribution, will result in sphere volumes between 20 and 220% of the initial value! Again, only minor influence of the tilt increments on the edge positions and the steepness has been observed, which is consistent with the results from global edge profiles.
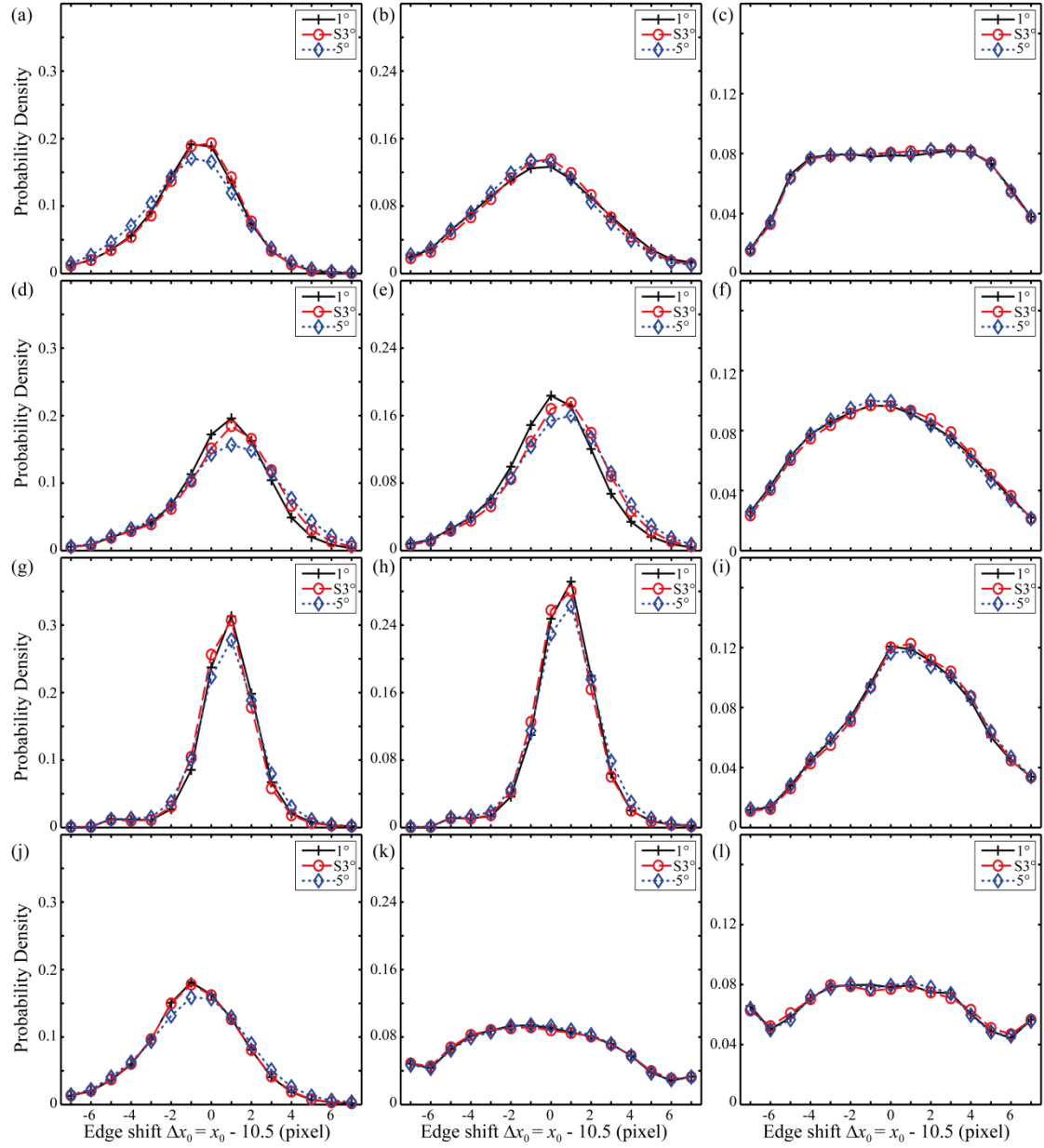
Figure 7. The probability density distribution of the edge shift Δx_0 characterized from local edge profiles along the X direction in the SIRT (a–c), TVM (d–f), DART (g–i), and WBP (j–l) reconstruction at a total electron dose 10^6 e/Å^2 (a,d,g,j), 10^4 e/Å^2 (b,e,h,k), and 10^2 e/Å^2 (c,f,i,l), with the tilt increments of 1°, 5°, and Saxton 3°.

In the TVM reconstruction, the probability distribution of edge positions at the total electron dose of 10^6 e/Å^2 ($\sigma_x \sim 2.06$) is similar to the distribution at the electron dose of 10^4 e/Å^2 ($\sigma_x \approx 2.08$ nm), as shown in Figure 7d,e. However, it becomes significantly widened ($\sigma_x \approx 3.35$ nm) as the electron dose reduces to 10^2 e/Å^2 (Figure 7f). In addition, the variation of edge shifts in the reconstructions at the total electron dose of 10^4 e/Å^2 and 10^6 e/Å^2 slightly increases as the tilt increments become larger. For instance, the mean and standard deviation in Figure 7e change from 0.75 ± 1.95 nm,

via 1.05 ± 2.06nm, to 1.23 ± 2.22nm as increase of the tilt increments from $1°$, via
Saxton $3°$, to $5°$.

In the DART reconstruction, the probability distribution of edge shifts is slightly
widened as the total electron dose decreases from 10^6 e/Å^2 to 10^4 e/Å^2, though the
mean edge shifts are similar (Figure 7g,h). Nevertheless, at the total electron dose of
10^2 e/Å^2, it is not only broadened but also significantly shifted into the object side, e.g.
1.40 ± 2.83 nm along the X direction (Figure 7i). In addition, the tilt increments have
an influence on the distribution of edge positions at a total electron dose of 10^4 e/Å^2
and 10^6 e/Å^2. Here, the variation using the Saxton $3°$ angular scheme has the smallest
and $5°$ constant increments the largest spread, i.e. $\sigma_x = 1.67$ nm and $\sigma_x = 2.02$ nm in
Figure 7g, respectively. It should be pointed out that the influence of tilt increments is
negligible in the reconstruction at a total electron dose of 10^2 e/Å^2, as can be seen in
Figure 7i.

For the WBP reconstruction, Figure 7 shows that the distribution of edge positions is
dramatically broadened as the decrease of the total electron dose. For example, the
standard deviation of the edge shifts in Z direction changes from 2.44 nm, via 3.68 nm,
to 4.14 nm as the total electron dose reduces from 10^6 e/Å^2, via 10^4 e/Å^2, to 10^2 e/Å^2.
It should be noted that only minor influence of the tilt increments on the distribution
of edge positions has been observed, as displayed in Figure 7j–l.

3.4 Gap profile

Figure 8 presents the difference Δw between the measured gap width w_m and the
actual gap width w_a along both the X and Z direction, i.e., $\Delta w = w_m - w_a$. A negative
value ($\Delta w < 0$) represents a narrowed gap whereas positive values ($\Delta w > 0$) represent a
broadened gap. Here we note that some global gap profiles in the Z direction contain
such low intensity variations that the Gaussian could not be fitted, thus leading to
blank data fields in Figure 8. Overall, there is a similar trend for all algorithms,
namely an increased precision with increasing gap width. This effect is best seen at a
total electron dose of 10^6 e/Å^2 (Figure 8a,b) where the measured gap width in the
SIRT, TVM, and WBP reconstructions converge towards the model when the gap
increases from 3 nm to 12 nm. Generally, 3 nm and 6 nm gaps are overestimated
using the three reconstruction methods. In the SIRT reconstruction, the smallest
difference between the ideal and measured gap is found in the 12 nm gap, i.e.,

$\Delta w_x = 0.5$ nm and, $\Delta w_z = -0.5$ nm. The 9 nm gaps in the WBP are well determined, whereas the 12 nm gaps are slightly underestimated. In the TVM reconstruction, the most accurate result has been found for the 12 nm gaps, but one needs to consider that the measured value strongly depends on the applied tilt scheme (especially along the X direction Figure 8a). In contrast, DART is the most accurate at small gap widths and more significantly underestimates 9 nm and 12 nm gaps. As can be seen in Figure 8c,d, similar measurements of gap widths have been obtained for the reconstruction at a total electron dose of 10^4 e/Å^2. Here we like to point out that the 3 nm gaps in the Z direction are barely resolved in the SIRT and WBP reconstructions (Figure 8b,d).

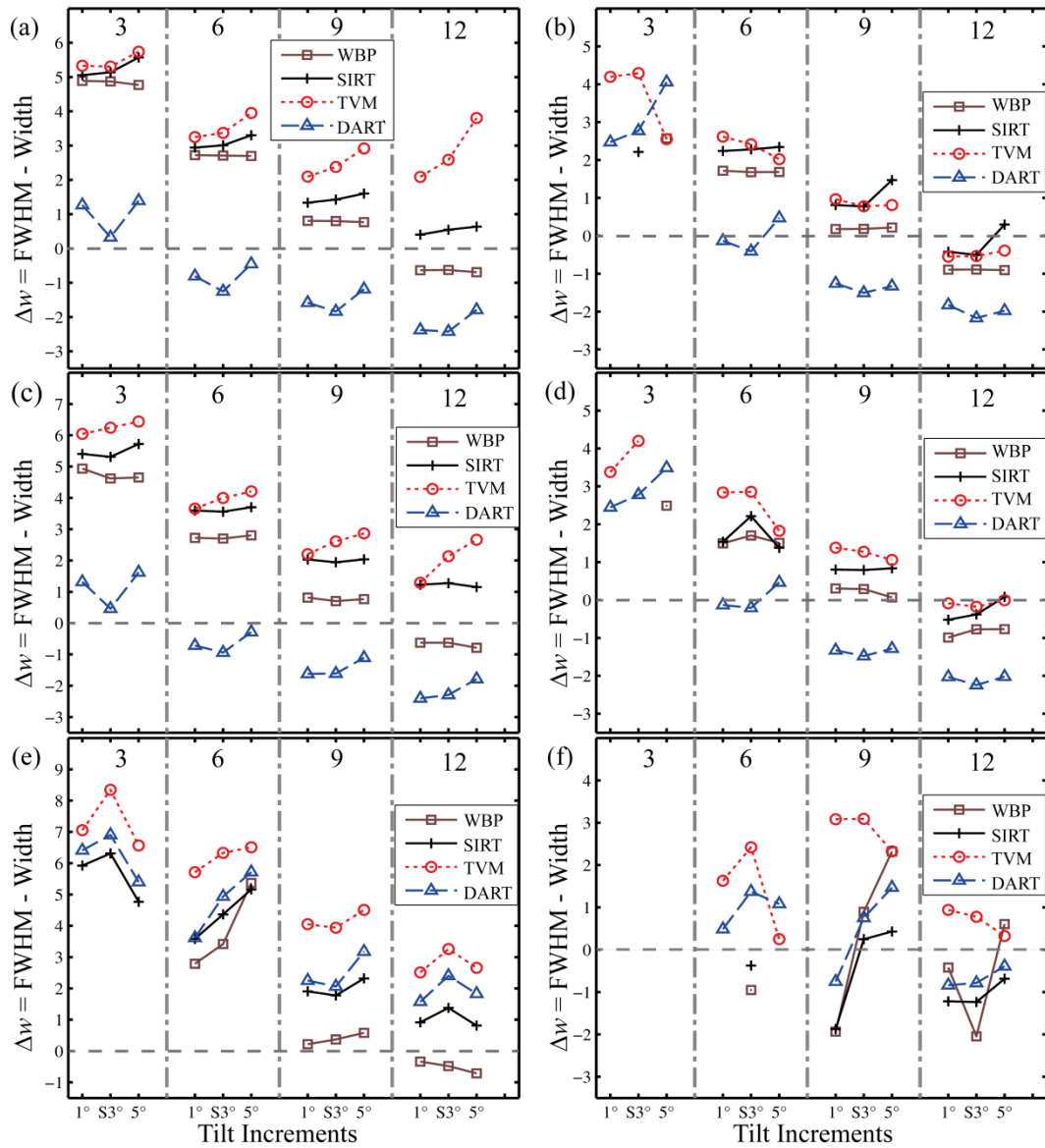Figure 8. The difference between the original and the measured gap width of the gap intensity profiles from the reconstruction with the total electron dose of 10^6 e/Å^2 (a, b), 10^4 e/Å^2 (c, d), and 10^2 e/Å^2 (e, f) along both the X (a, c, e) and Z (b, d, f) direction. Four different gap widths are studied, i.e. 3 nm (region 3), 6 nm (region 6), 9 nm (region 9), and 12 nm (region 12). Due

to too flat or chaotic behavior of the global edge profiles, in some condition the gap width cannot be determined, thus, leading to blank data points, for example, for the 3 nm gaps along the Z direction (f). S3° denotes the Saxton scheme with an angular starting interval of 3°.

In all the reconstructions at electron doses of 10^2 e/Å^2 (Figure 8e), the measured gap value converges to the model value when going from 3 nm to 12 nm along the X direction. It is found that the most accurate determined measurement is for the 9 nm gaps in the WBP. Nevertheless, 3 nm gaps in the WBP reconstruction along the X direction cannot be resolved because of too noisy data. Along the Z direction, only 9 nm and 12 nm gaps can be determined from all the reconstructions, while the 6 nm gaps can only be found in both TVM and DART reconstruction, or with SIRT and WBP but using a Saxton 3° tilt scheme. Three nanometer gaps along the Z direction cannot be determined from any reconstruction at the total electron dose of 10^2 e/Å^2.

4   Discussion and Conclusion

Although the SIRT, TVM and DART reconstruction methods have been compared before in the literature [22, 23, 32, 33], these studies are generally based on experimental data, lacking a detailed knowledge of the ground truth. In this work, we have simulated the electron tomography workflow based on a well–defined model of tubular domains in a matrix with slab geometry. The model was chosen as it closely resembles a large range of functional materials, such as a P3HT/PCBM bulk heterojunction thin–film or a CNT/polymer nanocomposite thin–section. In particular we investigated effects of a limited total electron dose and variations in tilt scheme on the properties of this three reconstruction methods. Both the advantages and disadvantages of the SIRT, TVM, and DART are quantitatively analyzed by comparing with the ground truth of the model. Our comparisons not only include the sharpness of the transitions between phases which provides an estimate of the achievable resolution, but also the position of interfaces and the size of gaps between objects which are key parameters in quantification of object morphologies and connectivity.

Expectedly, as the electron dose available for imaging decreases, the fidelity of all reconstruction methods decreases. We find that the SIRT algorithm is the least affected by variations in total dose and tilt scheme, which means that the fidelity of the SIRT reconstruction is preserved when using fewer projections. This is a clear

benefit for beam–sensitive specimens and if a large variety of imaging conditions or tilt schemes are utilized. The disadvantage is that the SIRT reconstruction suffers from a low SNR, and thus it needs extra efforts to denoise and segment the tomograms before it can be used for quantification. In contrast, TVM significantly reduces noise and sharpens transitions between materials which enables a simpler and easier segmentation of the reconstruction. However, objects in the TVM reconstruction become thinned as compared to the model, as illustrated by the measured edge shifts and the overestimation of gap sizes (Figure S11). Moreover, a significant dependence of TVM on the applied tilt scheme is observed, which indicates that with the presented measures a lower number of images (i.e., larger tilt increments) is not advised. This is an especially important point as this study cannot reproduce the general conclusions that compressive sensing approaches deal better with fewer projections [32, 33, 35]. The DART provides a binarized reconstruction and suppresses the elongation artifacts along the beam direction.

Here it is noteworthy that, at the total electron dose of 10^2 e/Å^2, the WBP yields a slightly better global resolution in comparison with the SIRT, TVM, and DART method, though it is also the noisiest reconstruction. The poor results for TVM and DART at this total dose are possibly related to the inappropriate l^2–norm in the data fit term which assumes a Gaussian distribution instead of a Poisson distribution for noise. Finally, one advantage of WBP and SIRT are their easier implementation and use, whereas TVM and DART are sensitive to the reconstruction parameters and require expert knowledge for properly setting regularization parameters or ratio of boundary pixels, respectively. In summary, to determine which of the many possible reconstruction approaches, such as WBP [13], SIRT [26], TVM [23], DART [22], ART [27], EST [60], Directt [61], W–SIRT [62], is best for a particular class of samples, a study as the one presented here for tubular domains in a slab matrix should be carried out.[1]

---

[1] Additional to the aspects discussed, experimental misalignment including magnification changes, image rotation, residual lateral and axial shifts, microscope and sample holder as well as alignment procedure used, affect the final result in practice. This can be taken into account, e.g. by taking into account an additional (Gaussian) distribution for the shifts and rotations, but since the settings for this are highly specific, we consider these effects as beyond the scope of the present investigation.

Acknowledgments

Supplementary Information

Supplementary data associated with this article can be found in the online version.

References

[1] H. Jinnai, R.J. Spontal, Transmission electron microtomography in polymer research, Polymer, 50 (2009) 1067-1087.

[2] H. Friedrich, P.E. de Jongh, A.J. Verkleij, K.P. de Jong, Electron tomography for heterogeneous catalysts and related nanostructured materials, Chem. Rev., 109 (2009) 1613-1629.

[3] R. Leary, P.A. Midgley, J.M. Thomas, Recent advances in the application of electron tomography to materials chemistry, Acc. Chem. Res., (2012).

[4] P.A. Midgley, R.E. Dunin-Borkowski, Electron tomography and holography in materials science, Nat. Mater., 8 (2009) 271-280.

[5] S.D. Oosterhout, M.M. Wienk, S.S. van Bavel, R. Thiedmann, L.J.A. Koster, J. Gilot, J. Loos, V. Schmidt, R.A.J. Janssen, The effect of three-dimensional morphology on the efficiency of hybrid polymer solar cells, Nat. Mater., 8 (2009) 818-824.

[6] S.S. van Bavel, E. Sourty, G. de With, J. Loos, Three-dimensional nanoscale organization of bulk heterojunction polymer solar cells, Nano Lett., 9 (2009) 507-513.

[7] H. Jinnai, R.J. Spontak, T. Nishi, Transmission electron microtomography and polymer nanostructures, Macromolecules, 43 (2010) 1675-1688.

[8] S. Bals, S. Van Aert, G. Van Tendeloo, High resolution electron tomography, Curr. Opin. Solid State Mater. Sci., 17 (2013) 107-114.

[9] J.J. Fernandez, Computational methods for materials characterization by electron tomography, Curr. Opin. Solid State Mater. Sci., 17 (2013) 93-106.

[10] L.F. Drummy, C. Kubel, Polymer microscopy: Current challenges, Polym. Rev. (Philadelphia, PA, U. S.), 50 (2010) 231-234.

[11] G. Van Tendeloo, S. Bals, S. Van Aert, J. Verbeeck, D. Van Dyck, Advanced electron microscopy for advanced materials, Adv. Mater., 24 (2012) 5655-5675.

[12] P.A. Midgley, M. Weyland, 3d electron microscopy in the physical sciences: The development of z-contrast and eftem tomography, Ultramicroscopy, 96 (2003) 413-431.

[13] M. Radermacher, Weighted back-projection methods, in: Electron tomography, Springer, 2006, pp. 245-273.

[14] C. Kubel, D. Niemeyer, R. Cieslinski, S. Rozeveld, Electron tomography of nanostructured materials - towards a quantitative 3d analysis with nanometer resolution, Thermec 2009, Pts 1-4, 638-642 (2010) 2517-2522.

[15] H. Friedrich, P.M. Frederik, G. de With, N.A.J.M. Sommerdijk, Imaging of self-assembled structures: Interpretation of tem and cryo-tem images, Angew. Chem., Int. Ed., 49 (2010) 7850-7858.

[16] R.F. Egerton, Control of radiation damage in the tem, Ultramicroscopy, 127 (2013) 100-108.

[17] P.K. Luther, Sample shrinkage and radiation damage of plastic sections, in: Electron tomography, Springer, 2006, pp. 17-48.

[18] P. Penczek, M. Marko, K. Buttle, J. Frank, Double-tilt electron tomography, Ultramicroscopy, 60 (1995) 393-410.

[19] D.N. Mastronarde, Dual-axis tomography: An approach with alignment methods that preserve resolution, J. Struct. Biol., 120 (1997) 343-352.

[20] N. Kawase, M. Kato, H. Nishioka, H. Jinnai, Transmission electron microtomography without the "missing wedge" for quantitative structural analysis, Ultramicroscopy, 107 (2007) 8-15.

[21] X.X. Ke, S. Bals, D. Cott, T. Hantschel, H. Bender, G. Van Tendeloo, Three-dimensional analysis of carbon nanotube networks in interconnects by electron tomography without missing wedge artifacts, Microsc. Microanal., 16 (2010) 210-217.

[22] K.J. Batenburg, S. Bals, J. Sijbers, C. Kubel, P.A. Midgley, J.C. Hernandez, U. Kaiser, E.R. Encina, E.A. Coronado, G. Van Tendeloo, 3d imaging of nanomaterials by discrete tomography, Ultramicroscopy, 109 (2009) 730-740.

[23] B. Goris, W. Van den Broek, K.J. Batenburg, H.H. Mezerji, S. Bals, Electron tomography based on a total variation minimization reconstruction technique, Ultramicroscopy, 113 (2012) 120-130.

[24] W.O. Saxton, W. Baumeister, M. Hahn, Three-dimensional reconstruction of imperfect two-dimensional crystals, Ultramicroscopy, 13 (1984) 57-70.

[25] A.C. Kak, M. Slaney, Principles of computerized tomographic imaging, Society for Industrial and Applied Mathematics, Philadelphia, 2001.

[26] P. Gilbert, Iterative methods for 3-dimensional reconstruction of an object from projections, J. Theor. Biol., 36 (1972) 105-117.

[27] R. Gordon, R. Bender, G.T. Herman, Algebraic reconstruction techniques (art) for 3-dimensional electron microscopy and x-ray photography, J. Theor. Biol., 29 (1970) 471-481.

[28] J.J. Fernandez, A.F. Lawrence, J. Roca, I. Garcia, M.H. Ellisman, J.M. Carazo, High-performance electron tomography of complex biological specimens, J. Struct. Biol., 138 (2002) 6-20.

[29] T.M. Benson, J. Gregor, Modified simultaneous iterative reconstruction technique, for faster parallel computation, 2005 IEEE Nuclear Science Symposium Conference Record, Vols 1-5, (2005) 2715-2718.

[30] S. Bals, K.J. Batenburg, J. Verbeeck, J. Sijbers, G. Van Tendeloo, Quantitative three-dimensional reconstruction of catalyst particles for bamboo-like carbon nanotubes, Nano Lett., 7 (2007) 3669-3674.

[31] S. Bals, K.J. Batenburg, D.D. Liang, O. Lebedev, G. Van Tendeloo, A. Aerts, J.A. Martens, C.E.A. Kirschhock, Quantitative three-dimensional modeling of zeotile through discrete electron tomography, J. Am. Chem. Soc., 131 (2009) 4769-4773.

[32] Z. Saghi, D.J. Holland, R. Leary, A. Falqui, G. Bertoni, A.J. Sederman, L.F. Gladden, P.A. Midgley, Three-dimensional morphology of iron oxide nanoparticles with reactive concave surfaces. A compressed sensing-electron tomography (cs-et) approach, Nano Lett., 11 (2011) 4666-4673.

[33] B. Goris, T. Roelandts, K.J. Batenburg, H.H. Mezerji, S. Bals, Advanced reconstruction algorithms for electron tomography: From comparison to combination, Ultramicroscopy, 127 (2013) 40-47.

[34] A.H. Andersen, A.C. Kak, Simultaneous algebraic reconstruction technique (sart) - a superior implementation of the art algorithm, Ultrason. Imaging, 6 (1984) 81-94.

[35] R. Leary, Z. Saghi, P.A. Midgley, D.J. Holland, Compressed sensing electron tomography, Ultramicroscopy, 131 (2013) 70-91.

[36] D.L. Chen, H. Friedrich, G. de With, On resolution in electron tomography of beam sensitive materials, J. Phys. Chem. C, 118 (2014) 1248-1257.

[37] T.M. Peters, Algorithms for fast back and re-projection in computed-tomography, IEEE Trans. Nucl. Sci., 28 (1981) 3641-3647.

[38] S.C.B. Lo, Strip and line path-integrals with a square pixel matrix - a unified theory for computational ct projections, IEEE Trans. Med. Imaging, 7 (1988) 355-363.

[39] F. Xu, K. Mueller, A comparative study of popular interpolation and integration methods for use in computed tomography, 2006 3rd Ieee International Symposium on Biomedical Imaging: Macro to Nano, Vols 1-3, (2006) 1252-1255.

[40] K.J. Batenburg, J. Sijbers, Dart: A practical reconstruction algorithm for discrete tomography, Ieee Transactions on Image Processing, 20 (2011) 2542-2553.

[41] X. Yang, J. Loos, Toward high-performance polymer solar cells: The importance of morphology control, Macromolecules, 40 (2007) 1353-1362.

[42] E.E. Tkalya, M. Ghislandi, G. de With, C.E. Koning, The use of surfactants for dispersing carbon nanotubes and graphene to make conductive nanocomposites, Curr. Opin. Colloid Interface Sci., 17 (2012) 225-232.

[43] K.B. Lu, E. Sourty, R. Guerra, G. Bar, J. Loos, Critical comparison of volume data obtained by different electron tomography techniques, Macromolecules, 43 (2010) 1444-1448.

[44] E.J. Kirkland, Advanced computing in electron microscopy, Springer, New York, 2010.

[45] M. Vulovic, R.B.G. Ravelli, L.J. van Vliet, A.J. Koster, I. Lazic, U. Lucken, H. Rullgard, O. Oktem, B. Rieger, Image formation modeling in cryo-electron microscopy, J. Struct. Biol., 183 (2013) 19-32.

[46] P.W. Hawkes, The electron microscope as a structure projector, Electron tomography: Threedimensional imaging with the

transmission electron microscope. Plenum Press: New York, (2006) 83-112.

[47]   L. Reimer, H. Kohl, Transmission electron microscopy : Physics of image formation, 5th ed., Springer, New York, NY, 2008.

[48]   W.J. Deruijter, Imaging properties and applications of slow-scan charge-coupled-device cameras suitable for electron-microscopy, Micron, 26 (1995) 247-275.

[49]   J.M. Zuo, Electron detection characteristics of a slow-scan ccd camera, imaging plates and film, and electron image restoration, Microsc. Res. Tech., 49 (2000) 245-268.

[50]   A.R. Faruqi, G. McMullan, Electronic detectors for electron microscopy, Q. Rev. Biophys., 44 (2011) 357-390.

[51]   W.O. Saxton, W. Baumeister, M. Hahn, 3-dimensional reconstruction of imperfect two-dimensional crystals, Ultramicroscopy, 13 (1984) 57-70.

[52]   J.C. Russ, The image processing handbook, CRC press, 2010.

[53]   R. Crowther, D. DeRosier, A. Klug, The reconstruction of a three-dimensional structure from projections and its application to electron microscopy, Proc. R. Soc. Lond. A., 317 (1970) 319-340.

[54]   W. Ming, M. Tian, R.D. van de Grampel, F. Melis, X. Jia, J. Loos, R. van der Linde, Low surface energy polymeric films from solventless liquid oligoesters and partially fluorinated isocyanates, Macromolecules, 35 (2002) 6920-6929.

[55]   N. Grossiord, O. Regev, J. Loos, J. Meuldijk, C.E. Koning, Time-dependent study of the exfoliation process of carbon nanotubes in aqueous dispersions by using uv-visible spectroscopy, Anal. Chem., 77 (2005) 5135-5139.

[56]   H. Heidari Mezerji, W. Van den Broek, S. Bals, A practical method to determine the effective resolution in incoherent experimental electron tomography, Ultramicroscopy, 111 (2011) 330-336.

[57]   A.J. Koster, M. Bárcena, Cryotomography: Low-dose automated tomography of frozen-hydrated specimens, in: Electron tomography, Springer, 2006, pp. 113-161.

[58]   M. Radermacher, 3-dimensional reconstruction of single particles from random and nonrandom tilt series, J. Electron Microsc. Tech., 9 (1988) 359-394.

[59]   N. Balakrishnan, Handbook of the logistic distribution, Dekker, 1992.

[60]   M.C. Scott, C.C. Chen, M. Mecklenburg, C. Zhu, R. Xu, P. Ercius, U. Dahmen, B.C. Regan, J.W. Miao, Electron tomography at 2.4-angstrom resolution, Nature, 483 (2012) 444-U491.

[61]   A. Lange, A. Kupsch, M.P. Hentschel, I. Manke, N. Kardjilov, T. Arlt, R. Grothausmann, Reconstruction of limited computed tomography data of fuel cell components using direct iterative reconstruction of computed tomography trajectories, J. Power Sources, 196 (2011) 5293-5298.

[62]   D. Wolf, A. Lubk, H. Lichte, Weighted simultaneous iterative reconstruction technique for single-axis tomography, Ultramicroscopy, 136 (2014) 15-25.

Supplementary Information:

2 **The properties of SIRT, TVM, and DART for 3D imaging of nanocomposite thin-films and sections**

4 Delei Chen[a,b], Bart Goris[c], Folkert Bleichrodt[d], Hamed Heidari Mezerji[c], Sara Bals[c], Kees Joost Batenburg[d], Gijsbertus de With[a], Heiner Friedrich[a,*]

6 [a] Laboratory of Materials and Interface Chemistry,

Department of Chemical Engineering and Chemistry,

8 Eindhoven University of Technology, Den Dolech 2,

5612 AZ, Eindhoven, The Netherlands

10 [b] Dutch Polymer Institute (DPI), P.O. Box 902, 5600 AX, Eindhoven, The Netherlands

12 [c] EMAT, University of Antwerp, Groenenborgerlaan 171, B-2020, Antwerp, Belgium

[d] Centrum Wiskunde & Informatica, Science Park 123, NL-1098XG, Amsterdam, The
14 Netherlands

* Corresponding author:

16 Dr. Heiner Friedrich, Phone: +31-40-247-3041, Email: h.friedrich@tue.nl

1 Materials and methods

1.1 Model definition
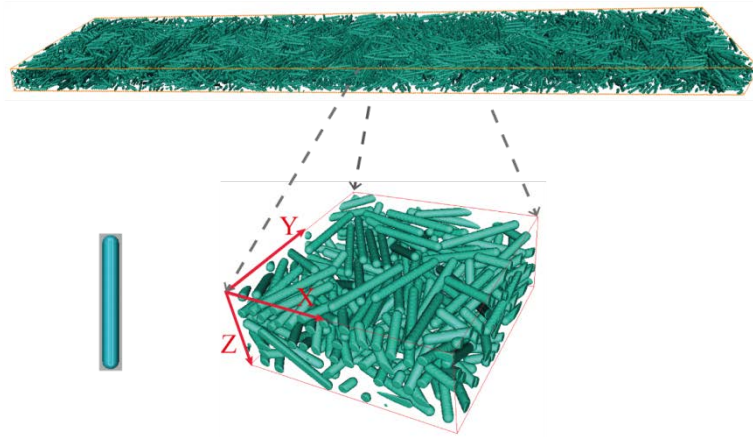
Figure S1. The full model system has a slab geometry (top), which is generated by randomly packing of single rods (bottom left). The rod-like filler particles such as P3HT nanowires or CNT's are approximated by cylinders with spherical end caps, of 200 pixels in length and 20 pixels in diameter with a sampling of 1 nm/pixel. The thickness of the matrix is 200 pixels. To ensure that the model covers the entire field of view (512×512) even at the tilt angle of 65°, the dimension of the full model was extended to 7430 pixels wide in X direction and 1024 pixels in Y direction (tilt axis). The volume fraction is set to 20% which results in 4360 rods randomly packed into the matrix. Please note that only the indicated (cut-out) region of interest will be reconstructed in electron tomography (bottom right).

1.2 Image formation

In electron microscopy, image formation can be sequentially divided into three steps: electron–specimen interaction, the optical system, and recording using a detector [1-3].

As an incident beam I_0 passes through a specimen with thickness t, interactions between them will arise. Sequentially, an initial 2D image (projection), is formed from the transmitted electrons, referred as an ideal projection which includes the information of the 3D specimen. Considering the electron–specimen interaction as mass–thickness contrast [3, 4], the intensity of the ideal projection can be calculated by the equation $I_t = I_0 \exp(-t/\varLambda_t)$, where $\varLambda_t$ is the mean–free–path (MFP) length of the specimen. The intensity I_0 is assumed as constant and given by the number of electrons per image, i.e., total dose divided by the number of images in the tilt series.

According to L. Reimer and H. Kohl, the MFP is determined by the contrast thickness $x_k(\alpha_o) = \rho \varLambda_t$, which is given by [4]:

$$\frac{1}{x_k(\alpha_o)} = \frac{4}{Zx_{el}} \left[\frac{Z-1}{4\left[1+(\alpha_o/\theta_0)^2\right]} + \ln \sqrt{1+(\theta_0/\alpha_o)^2} \right]$$

Eq. S1

In this equation, α_o (12.1 mrad) is the objective aperture, θ_0 (17.8 mrad for 300 keV) is characteristic angle, Z is the atomic number, ρ is the specimen (P3HT) density (1.1 g/cm^3), and x_{el} (114 µg/cm^2) is the elastic mean free path. Following this equation, the MFP is calculated, $\varLambda_t = 1087.2$ nm. It should be mentioned that in our case of a 200 nm polymer thin film, MFP, 1087.2 nm in P3HT imaged at 300 kV, is much larger than the effective beam path at the maximum tilt angle of 65°, thus one can safely assume that one works in the single scattering regime.

Next, the ideal projection is imaged by the electron optical system of the TEM into the detector plane, where the projection is blurred and referred to as filtered projection. In simulation, the electron optical system is commonly assumed to act as a convolution operator with a point spread function (PSF) $h(x,y)$ [1]. Mathematically, the filtered projection $I_b(x,y)$ is calculated from the convolution of the ideal projection $I_t(x,y)$ with the PSF $h(x,y)$, namely, $I_b(x,y) = I_t(x,y) \otimes h(x,y)$, where the symbol $\otimes$ represents convolution. For the sake of simplicity, a Gaussian function is employed to approximate the PSF of the optical system, namely,

$h(x,y) = (2\pi\sigma_b^2)^{-1}\exp(-(x^2+y^2)/2\sigma_b^2)$, where the σ_b is the blurring factor and determines

the maximum resolution. This blurring factor σ_b includes two sources. The first source

is from the diffraction–limited resolution σ_r which is an intrinsic limitation in

microscopy and determined by the wavelength λ, the focal length and the objective

aperture diameter. According to the Rayleigh criterion [5], the σ_r can be defined as

$\sigma_r = 1.22 f\lambda/D$, where f is the focal length and D is the aperture diameter of the

objective. Aberrations in the optical system, such as spherical aberration, chromatic

aberration, and the applied defocus result in an additional blurring factor σ_c. This

contribution is, in the first approximation, described by the contrast transfer function

(CTF):

$$CTF(q) = A(q)\sin 2\pi(\frac{1}{4}C_s\lambda q^2 - \frac{1}{2}\Delta z\lambda q^2) \qquad \text{Eq. S2}$$

where q is the spatial frequency in the reciprocal space, Δz is the defocus value, C_s is

the spherical aberration coefficient of the objective lens, and $A(q)$ is the aperture

function which is again given by the size of the objective aperture, $A(q) = 0$, if $q \le b$,

otherwise, $A(q) = 0$, where $b = D/(f\lambda)$ is the cut–off frequency. Notably, the CTF has a

oscillatory behavior which results in difficulties of interpreting high resolution

information on account of contrast inversions (see Figure S2).[6] The directly

interpretable passband extends from the origin to the spatial frequency q_0 at which the

first zero crossing of the CTF occurs.[7] Thus the effects of defocus and spherical

aberration, i.e. the blurring factor σ_c in the real space domain was for simplicity

assumed as $\sigma_c = 1/q_0$. The, total blurring σ_b can be treated approximately as:

$\sigma_b^2 = \sigma_r^2 + \sigma_c^2$. The effects of chromatic blur are commonly minimized experimentally

by zero–loss energy filtering and are, therefore, not taken into account.

Finally, the filtered projection is recorded by the TEM electron detector. The

recording process introduces shot noise and CCD noise in the final image [8-10]. Shot

noise is Poisson noise generated in the conversion process from electrons into photons

in the scintillator, denoted as $P_{oiss}(I_b(x,y))$. CCD noise $I_{CCD}(x,y)$ comes in during the

readout process, resulting from the dark current and readout noise, which is described

by a Gaussian distribution. The level of noise is determined from a dark image of a

Gatan MSC 794 camera as installed at the TU Eindhoven Cryo–Titan. The intensity

of the final projection $I(x,y)$ is calculated by adding both shot noise and CCD noise to the filtered projection, namely, $I(x,y) = P_{oiss}(I_b(x,y)) + I_{CCD}(x,y)$.
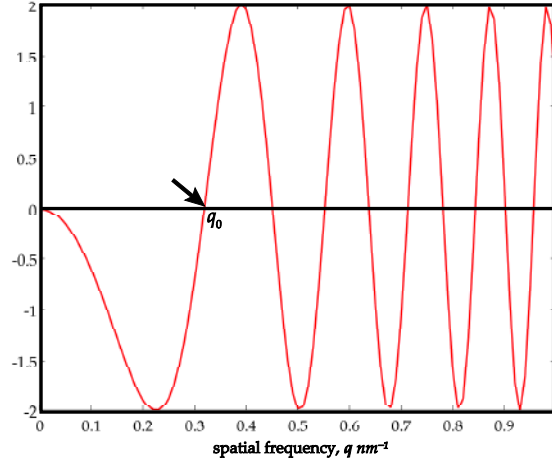

Figure S2. Plot of the contrast transfer function excluding spatial and temporal envelopes. The arrow points to the spatial frequency q_0 at which the first zero crossing of CTF occurs. The directly interpretable region is from the origin to q_0.

Table S1. TEM parameters used to calculate projections are based on TU/e Cryo–Titan.

Parameter	Symbol	Value	Unit
Acceleration Energy	E	300	keV
Objective aperture diameter	D	70	μm
Spherical aberration	C_s	3	mm
Chromatic aberration	C_c	3	mm
Focal length	f	2.89	mm
Under defocus	Δz	−5	μm
CCD noise	σ	0.17	e/pixel

1.3 Reconstruction information

In the SIRT reconstructions, the number of iterations was 10, 50, and 100 for accumulated electron dose of 10^2 e/Å^2, 10^4 e/Å^2, and 10^6 e/Å^2, respectively. These different iteration numbers are determined by visual inspection corresponding to our experimental experience. As the number of iterations increases, the reconstruction is gradually fitting to noise instead of the real object, thereby reducing the visibility and signal-to-noise ratio (SNR) in the reconstruction. For example, when using 50

5

iterations for a dose of 10^2, the visibility is markedly decreased, and the SNR drops from 0.8066 (for 10 iterations) to 0.4986. Additionally, the difference of projection error (χ^2) between 10 iterations and 50 iterations does change only ~ 3%.

In WBP, to reduce high frequency noise, a low–pass filter with a cut–off frequency set to 0.3 cycles/pixel and a Gaussian roll–off with sigma set to 0.05 is used, which is the same as the filter used in our previous work, see Reference 36 of the manuscript. According to Crowther's criterion, the resolution in the reconstruction is $\pi D/N$ = 200*π/131 = 4.794 pixels (0.209 cycles/pixel). Therefore, information or fine structures with a frequency larger than 0.3 cycles/pixel are not interpretable, and the cut–off frequency used here (0.3 cycles/pixel) is appropriate, and the cut–off frequency was chosen accordingly.

2 Results

2.1 Normalization of reconstructions

For the purpose of displaying all results next to each other in the figures, all raw reconstructions have been normalized so that they have the same mean density. For normalization let y_i denotes the grey value at the ith pixel in a raw reconstruction, the normalized grey value $\hat{y}_i$ is obtained from

$$\hat{y}_i = Ay_i + B$$

where $A = 1/(\mu_1 - \mu_0)$ and $B = -A\mu_0$ are scaling factor, and μ_1 and μ_0 are the mean density of objects and background in the raw reconstruction, respectively. Here we like to emphasize that the normalization procedure does not change the value of the derived parameters: steepness k and the edge position x_0, determined from the edge spread function ($S(x) = \frac{a}{2}[1 + \tanh k(x - x_0)] + b$).

Using the edge spread function, we have,

$$y_i = \frac{a}{2}[1 + \tanh k(x_i - x_0)] + b,$$

$$\hat{y}_i = \frac{\hat{a}}{2}[1 + \tanh \hat{k}(x_i - \hat{x}_0)] + \hat{b}$$

With the scaling factor A and B, the normalized grey value can be expressed as:

$$\hat{y}_i = Ay_i + B = A\left\{\frac{a}{2}[1 + \tanh k(x_i - x_0)] + b\right\} + B$$

$$= \frac{Aa}{2}[1 + \tanh k(x_i - x_0)] + Ab + B$$

$$= \frac{\hat{a}}{2}[1 + \tanh \hat{k}(x_i - \hat{x}_0)] + \hat{b}$$

Therefore, $\hat{a} = Aa$, $\hat{b} = Ab + B$, $\hat{k} = k$, and $\hat{x}_0 = x_0$.

Thus, the steepness and the edge position do not change with the normalization methods used.

7

2.2   Reconstruction results

Figure S3. An XZ numerical cross–section through the model (a), the SIRT (b), the TVM (c), and the DART (d) reconstructions at the total electron dose 10^2 e/Å^2 and the tilt increments of 1°.

As shown in Section 2.1 of the SI the absolute values of background (*b*) and dynamic range (*a*) do not affect the quantification results of edge position (x_0) and steepness (*k*). The artefact of horizontal striping acts as an extra noise on the edge profile along the Y direction only, and thus the noise variation along the Y direction is increased.
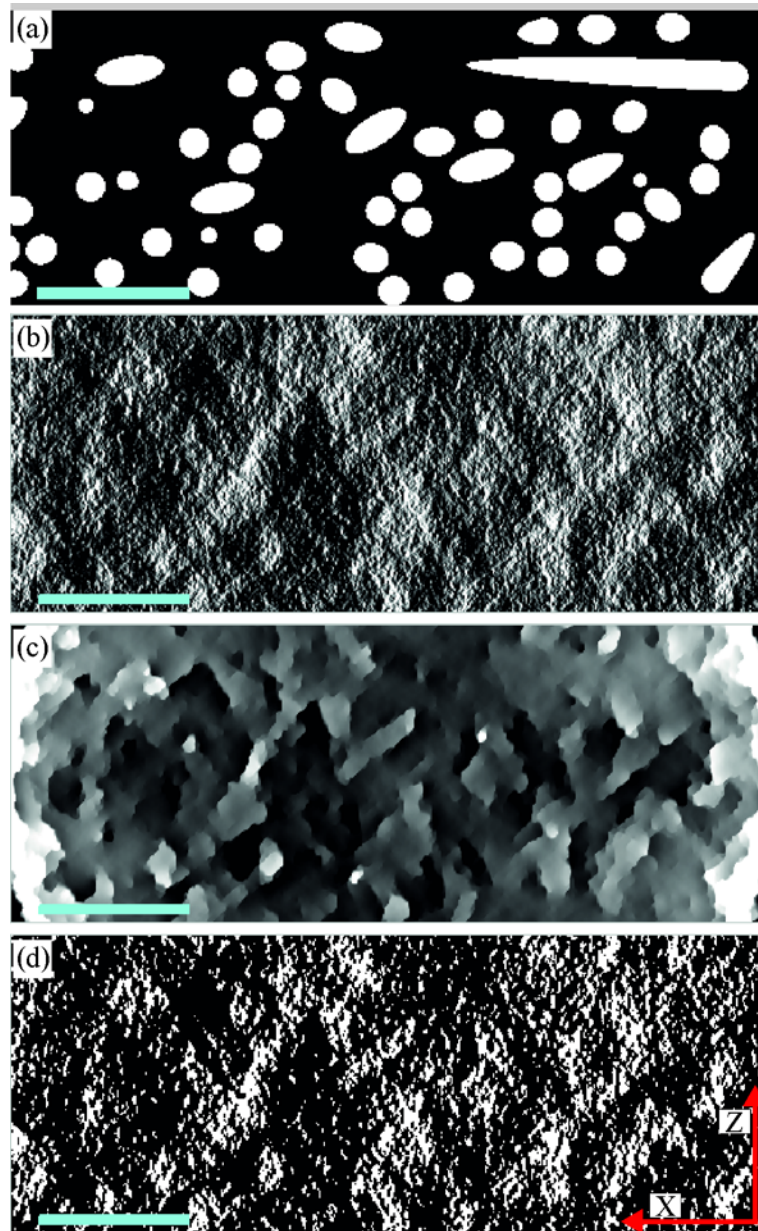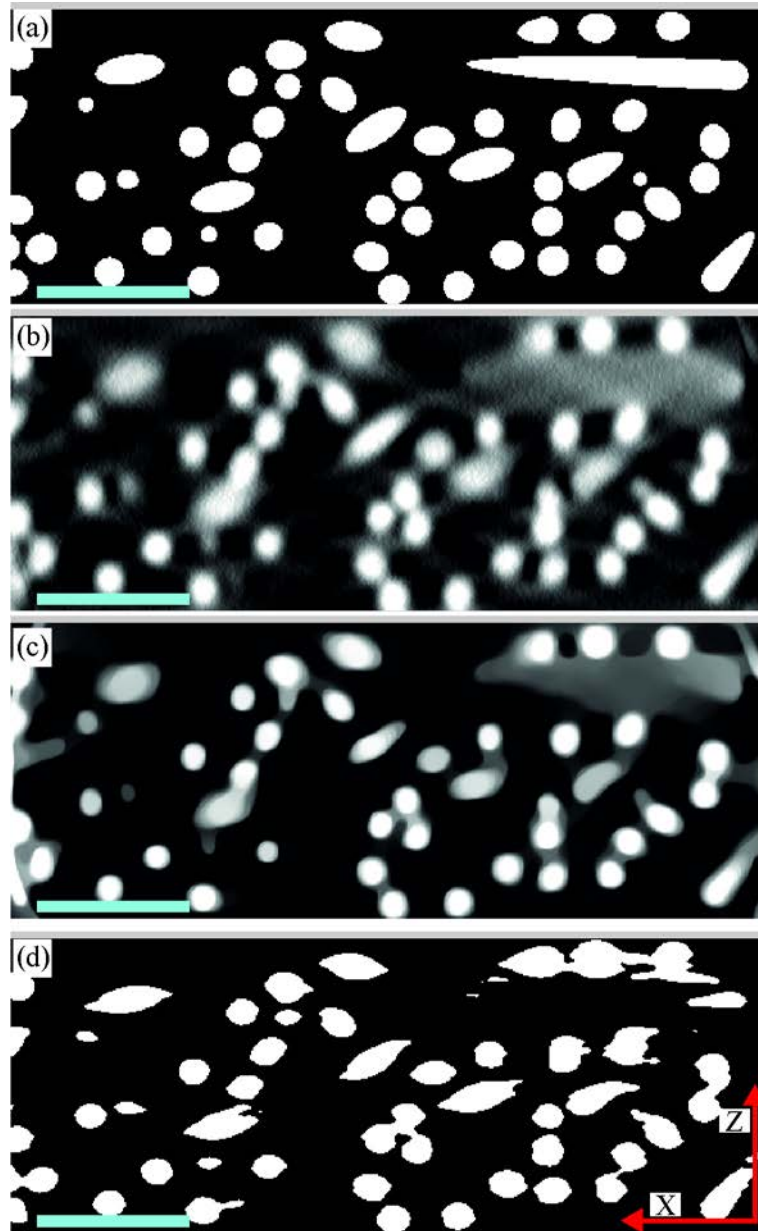
Figure S4. An XZ numerical cross–section through the model (a), the SIRT (b), the TVM (c), and the DART (d) reconstructions at the total electron dose of 10^6 e/Å^2 and the tilt increments of 1°.
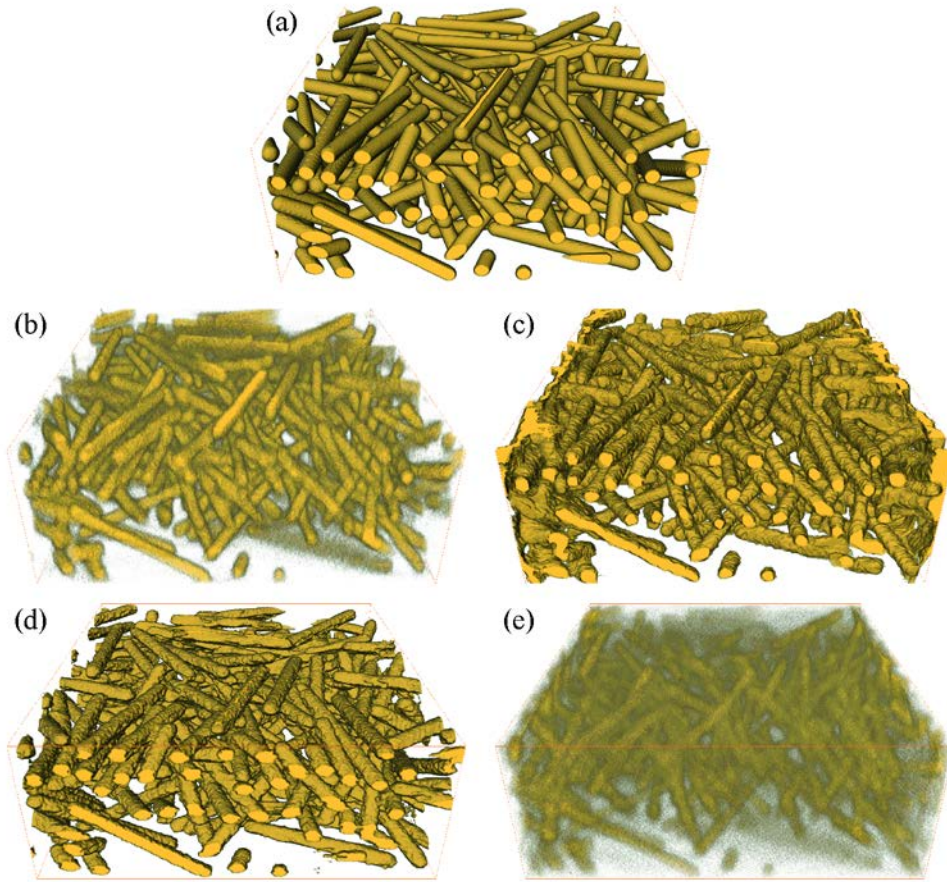
2   Figure S5. 3D volume rendering of the model (a) and the reconstruction using the SIRT (b), TVM (c), DART (d), and WBP (e) at the total electron does of 10^4 e/$\mathring{A}^2$ and the tilt
4   increments of $1°$. Because SIRT and WBP reconstructions contain a large number of small noise features, it results in a foggy or blurred appearance in (b) and (e). Owing to high SNR in
6   the TVM reconstruction and segmentation in the DART reconstruction, volume rendering of TVM and DART reconstructions is more similar to isosurface rendering.

8

2.3 Global edge profiles

Figure S6. The global edge profiles in the SIRT (*), TVM (o), DART (+), and WBP (Δ) reconstruction along the X direction, and the corresponding fitted line profile (dash lines). S3° denotes Saxton scheme with angular interval 3°.
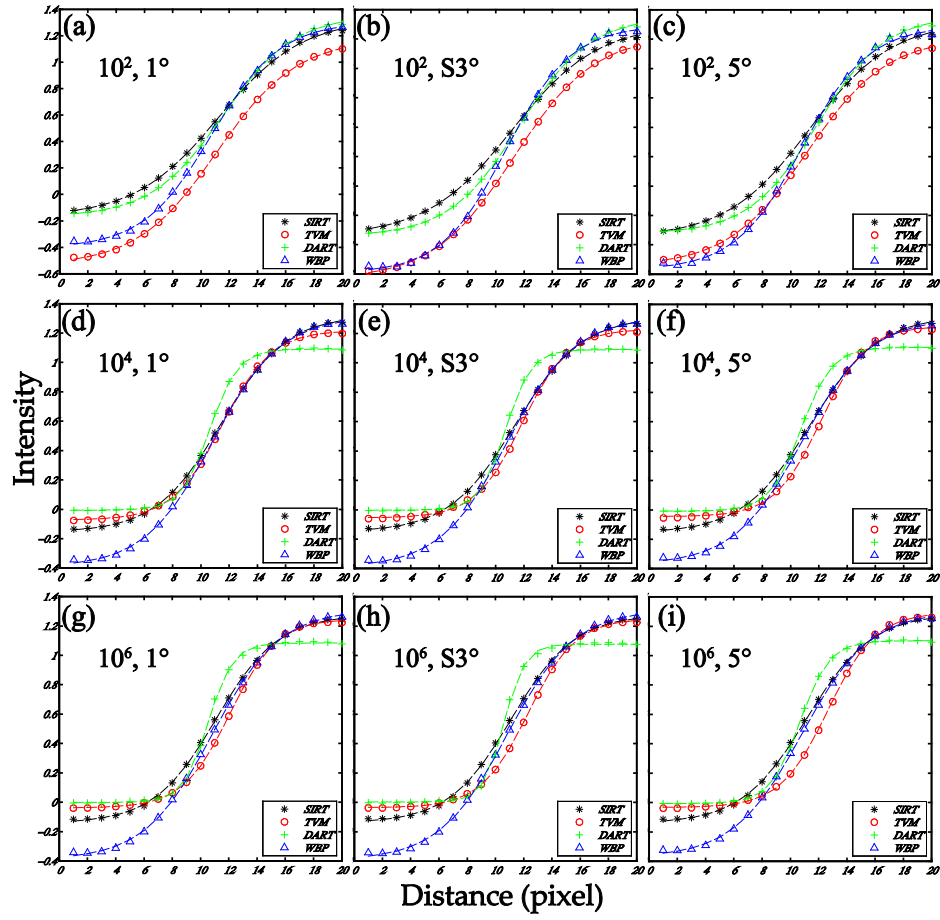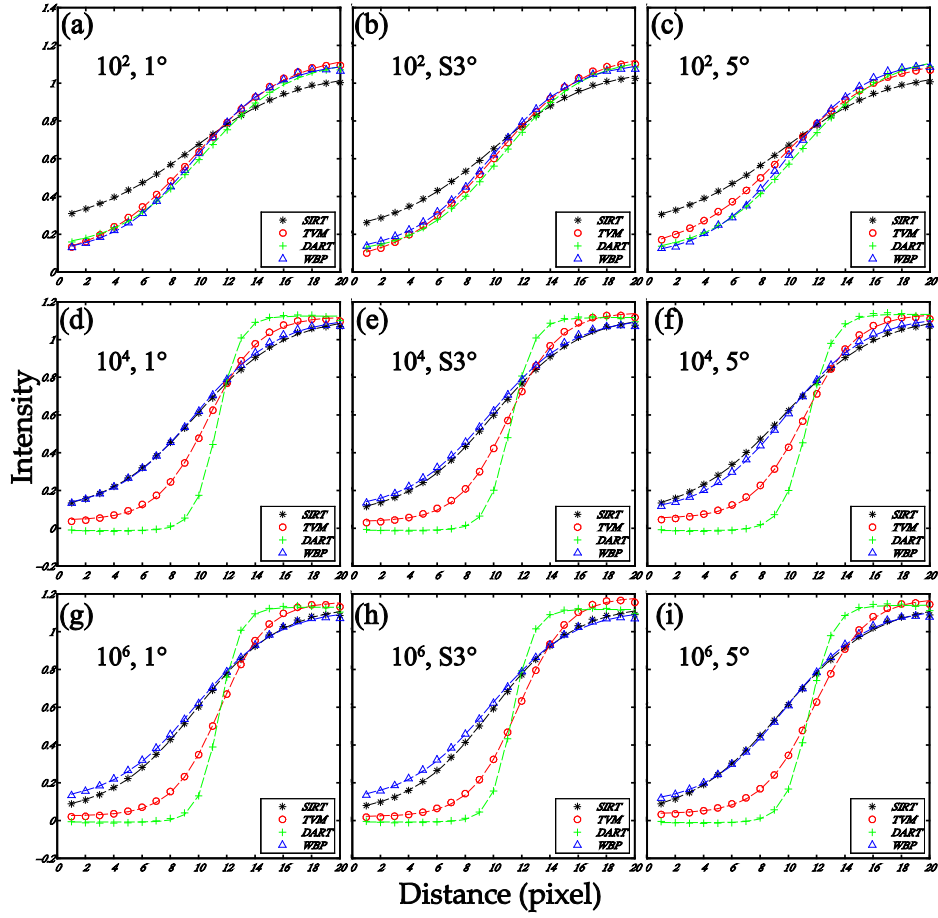
Figure S7. The global edge profiles in the SIRT (*), TVM (o), DART (+), and WBP (Δ) reconstruction along the Z direction, and the corresponding fitted line profile (dash lines).). S3° denotes Saxton scheme with angular interval 3°.

Table S2. Standard parameter errors of the steepness and the edge position and the goodness–of–fit (R^2) from the fitting of the global edge profiles in X and Z directions.
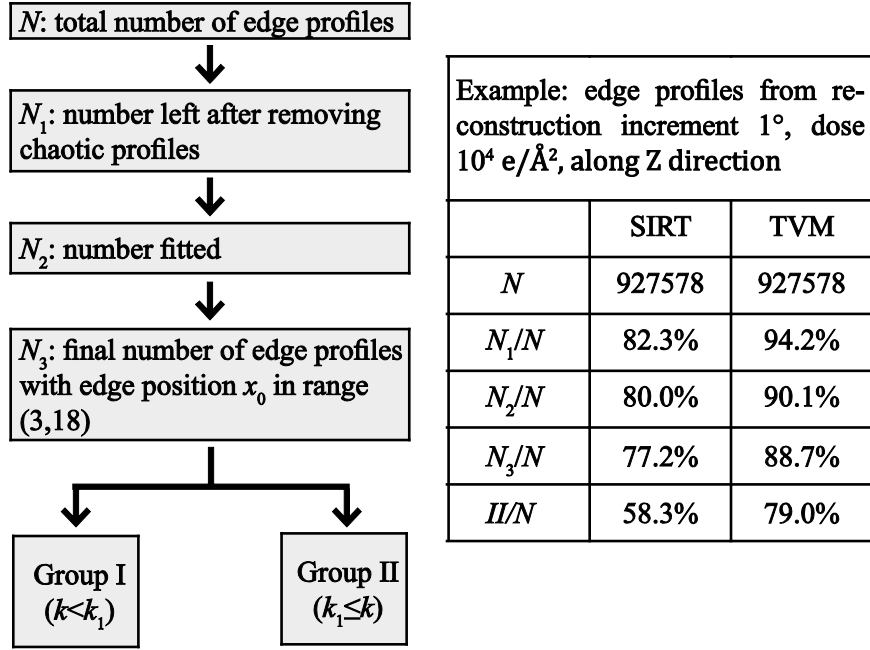
		SIRT			TVM			DART			WBP		
X		σ_k	σ_{x0}	R^2	σ_k	σ_{x0}	R^2	σ_k	σ_{x0}	R^2	σ_k	σ_{x0}	R^2
10^2	1°	0.003	0.034	0.9999	0.002	0.027	0.9999	0.003	0.031	0.9999	0.004	0.039	0.9998
	3°	0.003	0.042	0.9999	0.002	0.026	0.9999	0.003	0.035	0.9999	0.006	0.050	0.9996
	5°	0.004	0.045	0.9998	0.002	0.023	1.0000	0.004	0.041	0.9998	0.006	0.056	0.9996
10^4	1°	0.003	0.023	0.9999	0.003	0.020	0.9999	0.006	0.015	0.9999	0.004	0.041	0.9998
	3°	0.003	0.025	0.9999	0.004	0.024	0.9999	0.008	0.016	0.9999	0.005	0.043	0.9998
	5°	0.003	0.026	0.9999	0.005	0.029	0.9998	0.004	0.012	0.9999	0.004	0.038	0.9998
10^6	1°	0.004	0.038	0.9998	0.004	0.022	0.9999	0.015	0.028	0.9996	0.005	0.043	0.9997
	3°	0.004	0.039	0.9998	0.003	0.021	0.9999	0.020	0.026	0.9996	0.005	0.044	0.9997
	5°	0.004	0.037	0.9998	0.005	0.029	0.9998	0.006	0.016	0.9999	0.004	0.042	0.9998
Z													
10^2	1°	0.005	0.080	0.9997	0.005	0.076	0.9997	0.005	0.062	0.9997	0.006	0.073	0.9995
	3°	0.005	0.078	0.9997	0.006	0.072	0.9996	0.005	0.062	0.9996	0.005	0.055	0.9997
	5°	0.005	0.077	0.9997	0.005	0.069	0.9997	0.005	0.059	0.9997	0.006	0.069	0.9996
10^4	1°	0.005	0.064	0.9997	0.005	0.035	0.9997	0.012	0.017	0.9998	0.006	0.075	0.9995
	3°	0.005	0.061	0.9997	0.006	0.037	0.9997	0.011	0.016	0.9998	0.006	0.077	0.9995
	5°	0.005	0.067	0.9997	0.006	0.040	0.9997	0.012	0.022	0.9997	0.006	0.069	0.9995
10^6	1°	0.005	0.065	0.9996	0.006	0.032	0.9998	0.014	0.017	0.9998	0.006	0.076	0.9995
	3°	0.005	0.063	0.9997	0.005	0.033	0.9998	0.012	0.015	0.9998	0.006	0.077	0.9995
	5°	0.005	0.068	0.9997	0.005	0.035	0.9998	0.012	0.020	0.9998	0.006	0.072	0.9995

2

4

2.4   Procedure for analyzing the local edge profiles:

The intensity difference between background and object is in some of the local edge profiles imperceptible. As a result, many profiles cannot be fitted properly and should be disregarded. The classification procedure that was used to distinguish between suitable and non–suitable profiles for the edge spread function (ESF) fitting is schematically represented in Figure S8. In the first step we employ the t-test at a 0.05 significance level to examine all N profiles whether a significant difference between mean density of background μ_0 and object μ_1 in an individual edge profile exists, i.e. whether $\mu_0 < \mu_1$. If the difference is significant, the profile will be fitted to the edge spread function to find the four parameters, otherwise, it will be considered as chaotic and will be disregarded.

The fitting procedure for the remaining N_1 profiles employs the Levenberg-Marquardt algorithm which is an iterative technique. In most cases proper values for four parameters are obtained after $20 - 30$ iterations. We therefore set the maximum number of iterations to 100 and considered all solutions that would not be found after 100 iterations as unstable fittings and removed them, leaving over N_2 profiles. One should bear in mind that the number of accepted edge profiles is determined by the choice of the significance level and the number of the maximum iterations.

Finally, the fitting results are screened with respect to edge position and steepness. First, the edge position are restricted in the range (3,18) in order to ensure the edge profile always includes two phases (background and object) with respect to the 20 pixels length of the edge profile. Any solution of the edge position not in this range will be disregarded, leaving over N_3 profiles. Furthermore, the *FWHM* of the first derivative of the edge profile should be below 20 pixels because of the 20 pixels length of the profile. As a result, the minimum steepness, as defined by $k = 1.7627/FWHM$, is $k_1 = 1.7627/20 \cong 0.09$. The fitted results are divided into two groups with respect to steepness. The first group is the group of the edge profiles for which the steepness is less than k_1. In this group, the line profiles have no distinguishable transition between the background and the object, and therefore they will not be discussed further. The second group is the group of the edge profiles for which the steepness belongs to the range $[k_1, 10]$. Finally, we calculate the probability densities distribution for each parameter in groups II.

N: total number of edge profiles

↓

N_1: number left after removing chaotic profiles

↓

N_2: number fitted

↓

N_3: final number of edge profiles with edge position x_0 in range (3,18)

Group I ($k < k_1$)   Group II ($k_1 \leq k$)

Example: edge profiles from re-construction increment 1°, dose 10^4 e/Å², along Z direction

	SIRT	TVM
N	927578	927578
N_1/N	82.3%	94.2%
N_2/N	80.0%	90.1%
N_3/N	77.2%	88.7%
II/N	58.3%	79.0%

Figure S8. Procedure for analyzing the local edge profiles, N in total. Only the N_1 profiles fulfilling the t-test are fitted. Of these, only N_2 profiles remain which can be fitted properly with less than 100 iterations. The fitted edge profiles then are screened according to the constraints of edge positions $x_0 \in$ (3,18), resulting in N_3 remaining profiles. In the end, with respect to the steepness k, we divide the fitted results into two groups, an example results is shown on the right.

Table S3. The mean edge shifts Δx_0, standard error of the population mean (*SE*), and standard deviation σ of local edge profiles.

			SIRT			TVM			DART		
			X	Y	Z	X	Y	Z	X	Y	Z
10^2	1°	Δx_0	0.67	0.60	0.34	0.06	0.29	−0.26	1.30	1.12	0.84
		SE	0.0039	0.0039	0.0039	0.0037	0.0035	0.0037	0.0031	0.0033	0.0033
		σ	3.51	3.39	3.76	3.37	3.02	3.53	2.83	2.92	3.22
	S3°	Δx_0	0.64	0.64	0.37	0.15	0.43	−0.15	1.42	1.22	0.92
		SE	0.0039	0.0039	0.0039	0.0038	0.0035	0.0036	0.0031	0.0033	0.0033
		σ	3.52	3.36	3.72	3.38	3.02	3.51	2.83	2.91	3.19
	5°	Δx_0	0.72	0.68	0.35	0.12	0.51	−0.30	1.48	1.28	0.86
		SE	0.0038	0.0039	0.0039	0.0037	0.0034	0.0036	0.0031	0.0033	0.0034
		σ	3.47	3.36	3.74	3.31	2.95	3.50	2.83	2.90	3.25
	*	$\overline{\Delta x_0}$	0.68	0.64	0.35	0.11	0.41	−0.24	1.40	1.21	0.88
	*	$\overline{SE}$	0.0039	0.0039	0.0039	0.0037	0.0034	0.0036	0.0031	0.0033	0.0033
	*	$\bar{\sigma}$	3.50	3.37	3.74	3.35	2.99	3.51	2.83	2.91	3.22
10^4	1°	Δx_0	0.75	0.56	−0.45	0.75	0.67	−0.05	0.05	0.20	0.66
		SE	0.0025	0.0029	0.0039	0.0022	0.0024	0.0025	0.0022	0.0026	0.0017
		σ	2.25	2.53	3.07	1.95	2.13	2.42	1.95	2.29	1.68
	S3°	Δx_0	0.72	0.53	−0.43	1.05	0.97	0.29	0.10	0.22	0.57
		SE	0.0025	0.0028	0.0031	0.0023	0.0026	0.0026	0.0020	0.0025	0.0017
		σ	2.23	2.46	2.95	2.06	2.23	2.49	1.83	2.20	1.68
	5°	Δx_0	0.65	0.45	−0.65	1.23	1.17	0.33	0.13	0.23	0.67
		SE	0.0024	0.0028	0.0031	0.0025	0.0027	0.0027	0.0023	0.0027	0.0019
		σ	2.20	2.44	2.97	2.22	2.37	2.64	2.05	2.38	1.82
	*	$\overline{\Delta x_0}$	0.71	0.51	−0.51	1.01	0.94	0.19	0.09	0.22	0.63
	*	$\overline{SE}$	0.0025	0.0028	0.0031	0.0023	0.0026	0.0026	0.0022	0.0026	0.0018
	*	$\bar{\sigma}$	2.23	2.48	2.99	2.08	2.24	2.51	1.94	2.29	1.73
10^6	1°	Δx_0	0.24	0.07	−0.88	1.16	1.09	0.53	−0.03	0.11	0.76
		SE	0.0018	0.0023	0.0023	0.0021	0.0026	0.0024	0.0020	0.0026	0.0017
		σ	1.64	1.98	2.24	1.89	2.23	2.34	1.81	2.27	1.66
	S3°	Δx_0	0.27	0.08	−0.83	1.33	1.25	0.77	0.03	0.17	0.66
		SE	0.0018	0.0023	0.0023	0.0022	0.0027	0.0025	0.0019	0.0025	0.0017
		σ	1.62	1.97	2.23	1.99	2.35	2.45	1.67	2.14	1.63
	5°	Δx_0	0.23	0.05	−1.05	1.63	1.46	0.82	0.07	0.19	0.76
		SE	0.0020	0.0024	0.0025	0.0025	0.0029	0.0028	0.0022	0.0027	0.0019
		σ	1.81	2.09	2.43	2.28	2.52	2.66	2.02	2.40	1.80
	*	$\overline{\Delta x_0}$	0.24	0.07	-0.92	1.37	1.26	0.71	0.03	0.15	0.73
	*	$\overline{SE}$	0.0019	0.0023	0.0024	0.0023	0.0027	0.0026	0.0020	0.0026	0.0018
	*	$\bar{\sigma}$	1.69	2.01	2.30	2.06	2.37	2.49	1.83	2.27	1.70

* The averaged edge shifts $\overline{\Delta x_0}$, standard error of the population mean $\overline{SE}$, and standard deviation $\bar{\sigma}$ are calculated by averaging the corresponding values at the same electron dose from three different tilt increments for reference.
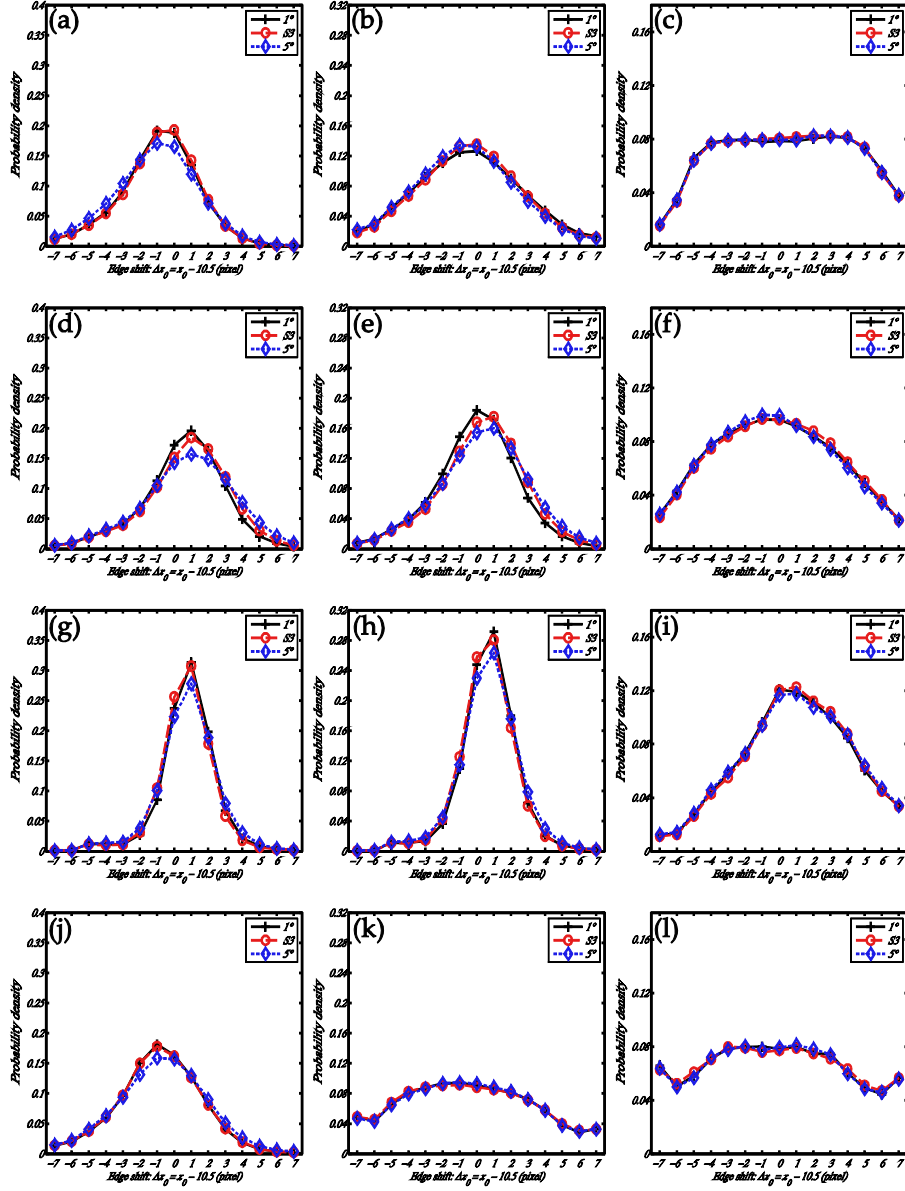
2   Figure S9. The probability density distribution of the edge shift Δx_0 characterized from local edge profiles along the Z direction in the SIRT (a-c), TVM (d-f), DART (g-i), and WBP (j-l)

4   reconstruction at a total electron dose 10^6 e/Å^2 (a,d,g,j), 10^4 e/Å^2 (b,e,h,k), and 10^2 e/Å^2 (c,f,i,l), with the tilt increments of 1°, 5°, and Saxton 3°.
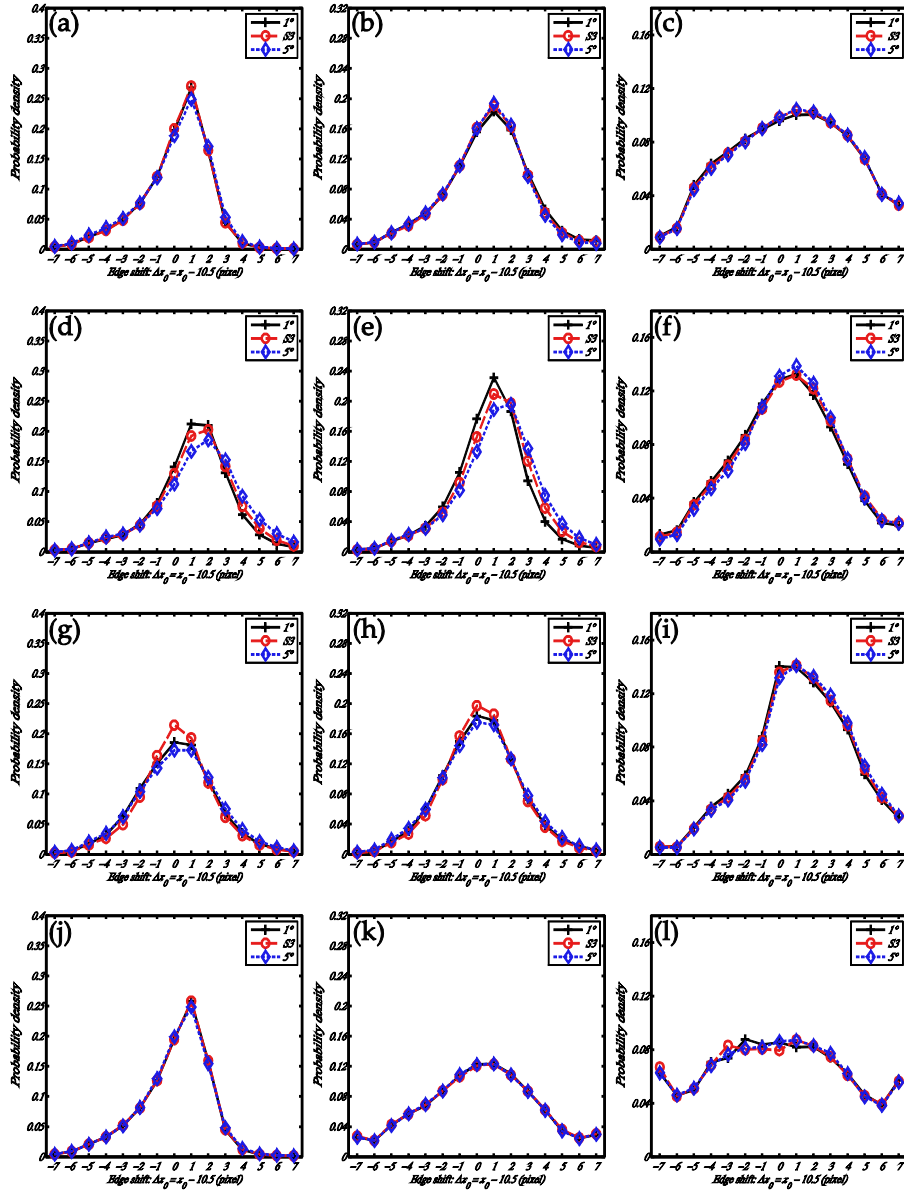
Figure S10. The probability density distribution of the edge shift Δx_0 characterized from local edge profiles along the Y direction in the SIRT (a-c), TVM (d-f), DART (g-i), and WBP (j-l) reconstruction at a total electron dose 10^6 e/Å^2 (a,d,g,j), 10^4 e/Å^2 (b,e,h,k), and 10^2 e/Å^2 (c,f,i,l), with the tilt increments of 1°, 5°, and Saxton 3°.
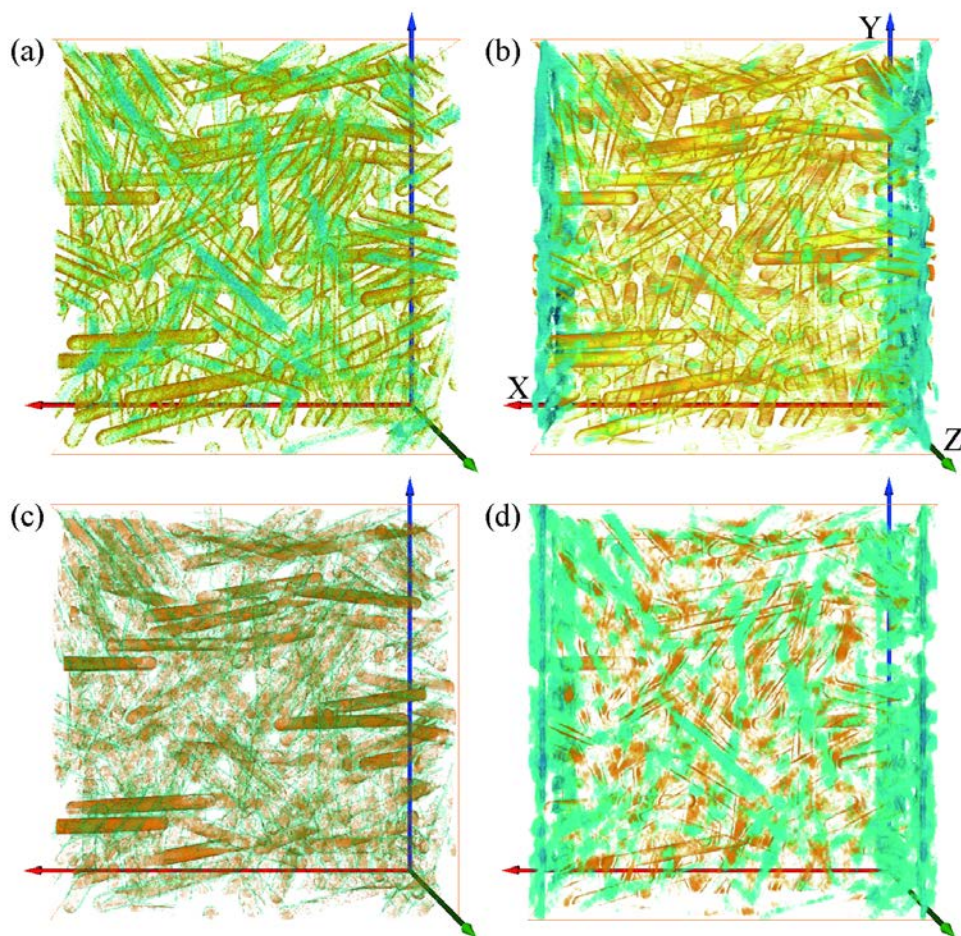
Figure S11 Volume rendering of the difference between the model and the reconstruction using (a) SIRT, (b), TVM, (c), DART, and (d) WBP methods. Blue area indicates over-reconstruction, i.e. particles extended; brown area indicates under-reconstructed, i.e., particles shrunk.

References

[1]   E.J. Kirkland, Advanced computing in electron microscopy, Springer, New York, 2010.

[2]   M. Vulovic, R.B.G. Ravelli, L.J. van Vliet, A.J. Koster, I. Lazic, U. Lucken, H. Rullgard, O. Oktem, B. Rieger, Image formation modeling in cryo-electron microscopy, J. Struct. Biol., 183 (2013) 19-32.

[3]   P.W. Hawkes, The electron microscope as a structure projector, Electron tomography: Threedimensional imaging with the transmission electron microscope. Plenum Press: New York, (2006) 83-112.

[4]   L. Reimer, H. Kohl, Transmission electron microscopy : Physics of image formation, 5th ed., Springer, New York, NY, 2008.

[5]   M. Born, E. Wolf, Principles of optics: Electromagnetic theory of propagation, interference and diffraction of light, CUP Archive, 1999.

[6]   D.B. Williams, C.B. Carter, Transmission electron microscopy : A textbook for materials science, 2nd ed., Springer, New York ; London, 2008.

[7]   J.X. Loos, How ovid remythologizes greek astronomy in 'metamorphoses' 1.747-2.400, Mnemosyne, 61 (2008) 257-289.

[8]   W.J. Deruijter, Imaging properties and applications of slow-scan charge-coupled-device cameras suitable for electron-microscopy, Micron, 26 (1995) 247-275.

[9]   J.M. Zuo, Electron detection characteristics of a slow-scan ccd camera, imaging plates and film, and electron image restoration, Microsc. Res. Tech., 49 (2000) 245-268.

[10]   A.R. Faruqi, G. McMullan, Electronic detectors for electron microscopy, Q. Rev. Biophys., 44 (2011) 357-390.